J. Fluid Mech. (2025), *vol.* 1006, A18, doi:10.1017/jfm.2025.9

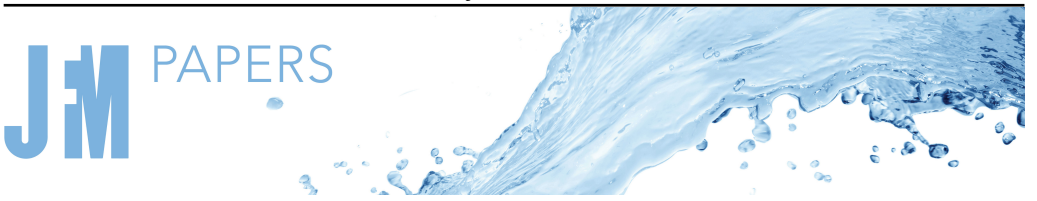

Optimally time-dependent modes of vortex gust–airfoil interactions

Yonghong Zhong[1], **Alireza Amiri-Margavi**[2], **Hessam Babaee**[2] and **Kunihiko Taira**[1]

[1]Department of Mechanical and Aerospace Engineering, University of California, Los Angeles, CA 90095, USA

[2]Department of Mechanical Engineering and Materials Science, University of Pittsburgh, Pittsburgh, PA15260, USA

Corresponding author: Yonghong Zhong, yhzhong@g.ucla.edu

(Received 19 June 2024; revised 14 December 2024; accepted 24 December 2024)

We find the optimally time-dependent (OTD) orthogonal modes about a time-varying flow generated by a strong gust vortex impacting a NACA 0012 airfoil. This OTD analysis reveals the amplification characteristics of perturbations about the unsteady base flow and their amplified spatiotemporal structures that evolve over time. We consider four time-varying laminar base flows in which a vortex with a strength corresponding to the gust ratio G of $\{-1, -0.5, 0.5, 1\}$ impinges on the leading edge of the airfoil at an angle of attack of 12°. In these cases, the impingement of the strong gust vortex causes massive separation and the generation of large-scale vortices around the airfoil within two convective time units. As these flow structures develop around the airfoil on a short time scale, the airfoil experiences large transient vortical lift variations in the positive and negative directions that are approximately five to ten times larger than the baseline lift. The highly unsteady nature of these vortex–airfoil interactions necessitates an advanced analytical technique capable of capturing the transient perturbation dynamics. For each of the considered gust ratios, the OTD analysis identifies the most amplified region to perturbations, the location of which changes as the wake evolves differently. For interactions between a moderate positive vortex gust ($G = 0.5$) and the airfoil, the area where perturbations are amplified transitions from the leading-edge vortex (LEV) sheet to the forming LEV. Later, this most amplified structure becomes supported in the airfoil wake directly behind the trailing edge. In contrast, a strong vortex gust ($G = \pm 1$) encountered by the airfoil shows the most amplified OTD mode to appear around the core of the shed vortices. This study provides an analysis technique and fundamental insights into the broader family of unsteady aerodynamic problems.

Key words: flow–structure interactions, nonlinear instability

1. Introduction

Flying in a gusty environment is challenging because wings can experience massive flow separation and violent transient force fluctuations. One critical gust parameter is the relative velocity between the gust and the free stream, often referred to as the gust ratio G (Jones 2020). The gust ratio indicates how strong a gust is; a larger-amplitude gust is likely to incite more intense flow efforts on a flying body. In nature, the profile and strength of aerodynamic disturbances can vary significantly depending upon the environment of interest. For these reasons, previous studies have considered transient gusts, including streamwise gusts, transverse gusts and vortex gusts. Among these various types of gusts, a spanwise vortex-gust elicits perhaps the most fluctuations in lift. When such a gust interacts with an airfoil, the resulting dynamics is transient and nonlinear, posing considerable challenges in understanding the unsteady flow behaviour. However, it is crucial to understand such effects that large-amplitude vortex gusts pose on flying bodies.

Unsteady aerodynamic models have been developed to capture the dominant effects of gust–airfoil interaction. For small-amplitude gust encounters where attached flow is assumed around the airfoil, linear thin airfoil theory and its extensions have been used to build theoretical models for both discrete (von Kármán & Sears 1938; Sears 1941) and periodic (Atassi 1984) gust disturbances. In fact, linear aerodynamic models such as the Küssner model have been known to be effective for a variety of disturbances, including cases where gust-induced flow separation occurs (Küssner 1936; Badrya *et al.* 2021). However, linear models become less accurate when the gust ratio is larger than 0.5 or when the angle of attack is higher than 20° in which case nonlinear effects are significant. While advancements in theoretical and analytical models have been made, characterizing the detailed transient gust–airfoil interactions in a global manner remains elusive due to the high dimensionality of the full-order problem.

To capture the dynamics of global flow fields, modal analysis is a useful tool that extracts dominant features of high-dimensional flows. For example, proper orthogonal decomposition (Lumley 1967; Aubry *et al.* 1988) identifies spatially energetic modes, and dynamic mode decomposition (Schmid 2010) extracts spatial structures that are associated with the spectral content of flow dynamics. Modal analysis can also reveal the stability and transition characteristics of fluid flows. Global stability analysis (Theofilis 2011) reveals the dominant stability modes from the linearized Navier–Stokes equations about a given steady state. The linear eigenvalues found from the global stability analysis provide information about the growth or decay rates of perturbations with respect to the base flow. Based on an energy measure for the time-dependent response of the flow (Schmid 2007), the non-modal analysis framework can evaluate energy amplification by analysing the harmonic response from harmonic forcing inputs (Farrell & Ioannou 1993) and formulate an initial-value problem to examine the transient energy growth over a finite time interval (Blackburn, Barkley & Sherwin 2008). Resolvent analysis (Trefethen *et al.* 1993; Jovanović & Bamieh 2005) is a method for understanding the response of a dynamical system to external forcing or perturbations. The response and forcing modes obtained from the resolvent analysis reveal the most amplified perturbation structures and how they are excited by external forcing. The resolvent analysis was extended for turbulent flows by treating the nonlinearity in the perturbation equation as

forcing (McKeon & Sharma 2010). The coherent structures identified by resolvent analysis provide physical interpretations in wall turbulence (Moarref *et al.* 2013) and turbulent cavity flows (Gómez *et al.* 2016). These modal techniques can provide fundamental behaviour of the flow response, which can help us understand turbulent flows and implement flow control (Yeh & Taira 2019; Liu *et al.* 2021).

Although the aforementioned modal analysis techniques offer valuable insights into the characterization of complex fluid flows (Taira *et al.* 2017; Unnikrishnan 2023), the majority of these methods are built on the assumption of a time-invariant base flow. These analysis techniques require careful generalization for analysing unsteady base flows. To address this issue, optimally time-dependent (OTD) mode decomposition (Babaee & Sapsis 2016) has been developed, where linear stability analysis can be performed for perturbation growth around arbitrarily time-dependent base flows. In particular, the OTD analysis is applied to the instantaneously linearized dynamics, and an evolution equation is derived for a set of orthonormal time-dependent modes. It has been shown that the OTD modes converge exponentially fast to the dominant eigenvectors associated with the largest finite-time Lyapunov exponents (Babaee *et al.* 2017). The OTD mode decomposition is closely related to dynamical low-rank approximation (Koch & Lubich 2007) and dynamically orthogonal decomposition (Sapsis & Lermusiaux 2009). The OTD method uncovers the time-dependent orthonormal modes that capture the dominant transient amplification of perturbations with respect to time-varying base flows, hence serves as a powerful tool to characterize the perturbation dynamics of various unsteady flows (Kern, Hanifi & Henningson 2022; Donello, Carpenter & Babaee 2022; Beneitez *et al.* 2023; Amiri-Margavi & Babaee 2024; Kern *et al.* 2024).

In this study, we employ OTD mode analysis to investigate vortex–airfoil interactions, where the vortex gust ratio magnitude exceeds 0.5. The complexity of such interactions, characterized by strong nonlinearities, transient dynamics and high-dimensional flow structures, demands a method that can adaptively capture perturbation dynamics of the evolving flow field. The OTD modes, which are found at each time step, offer a dynamic approach for dimensionality reduction and reveal the optimal timing and locations of critical perturbation amplifications. This makes OTD mode analysis particularly suited for studying the violent aerodynamic phenomena associated with large vortex gusts, where traditional methods fall short in capturing the essential dynamics.

By capturing the evolving flow structures and identifying regions of sensitivity at precise moments in time, OTD mode analysis enables the possibility of designing highly effective, time-varying flow control strategies. This dynamic approach to flow manipulation is critical for optimizing aerodynamic performance and mitigating adverse flow effects. For example, Blanchard & Sapsis (2019*b*) proposed a strategy for identifying the optimal control domain using a criterion derived from the OTD modes. They demonstrated that OTD-based control can successfully alleviate the flow unsteadiness by guiding flow trajectories towards the desired fixed point.

The current study is organized as follows. We start § 2 by presenting the methodology of OTD analysis. The model problem of vortex–airfoil interactions and the related physics are described in § 3. In § 4, the amplifications of perturbations for four vortex–airfoil interaction cases are examined with the OTD analysis. Finally, the conclusions are presented in § 5.

2. Methodology: OTD mode analysis

Our objective is to find the dominant transient amplification mechanisms of non-periodic time-dependent flows using the OTD mode analysis (Babaee & Sapsis 2016).

To identify the transient amplification of perturbations about an unsteady vortex gust–airfoil interactions, we consider the flow state $\mathbf{q}(t)$ to be comprised of the base flow trajectory $\bar{\mathbf{q}}(t)$ and perturbation $\mathbf{q}'(t)$,

$$\mathbf{q}(t) = \bar{\mathbf{q}}(t) + \mathbf{q}'(t) \in \mathbb{R}^n. \tag{2.1}$$

Here, it is assumed that the flow domain is spatially discretized, and n is the degree of the freedom of the discretized flow, i.e. the number of grid points times the number of state variables $(\rho, \rho u, \rho v, \rho w, e)$. We substitute this flow expression into the Navier–Stokes equations to derive the linear evolution equation for the perturbation $\mathbf{q}'(t)$ about an arbitrary trajectory $\bar{\mathbf{q}}(t)$. With the assumption that the perturbation magnitude is small, we find that

$$\frac{\mathrm{d}\mathbf{q}'(t)}{\mathrm{d}t} = \mathbf{L}_{\bar{\mathbf{q}}}(t)\mathbf{q}'(t). \tag{2.2}$$

The time-varying linear operator $\mathbf{L}_{\bar{\mathbf{q}}}(t) \in \mathbb{R}^{n\times n}$ is derived about the unsteady base state $\bar{\mathbf{q}}(t)$. For convenience, we drop the subscript from $\mathbf{L}_{\bar{q}}(t)$ and denote it as $\mathbf{L}(t)$.

In this paper, we take the base state $\bar{\mathbf{q}}(t)$ to be the unsteady flow produced by a gust vortex impinging on an airfoil. Through the present analysis, we aim to identify the dominant temporary evolving spatial structures susceptible to amplification during the vortex–airfoil interaction. The dynamics of the unsteady base flows will be discussed in § 3.2.

Now, we consider a collection of d initial perturbations

$$\mathbf{Q}'(t_0) \equiv [\mathbf{q}'_1(t_0), \mathbf{q}'_2(t_0), \ldots, \mathbf{q}'_d(t_0)] \in \mathbb{R}^{n\times \mathrm{d}}$$

and evolve them over time using linear equation (2.2) such that

$$\frac{\mathrm{d}\mathbf{Q}'(t)}{\mathrm{d}t} = \mathbf{L}(t)\mathbf{Q}'(t). \tag{2.3}$$

The aim here is to take the collection of perturbation trajectories $\mathbf{Q}'(t)$ that dynamically evolve about the time-varying base state $\bar{\mathbf{q}}(t)$ and determine the dominant modes that capture their time-varying amplification characteristics. To approximate the perturbations $\mathbf{Q}'(t)$ in a reduced-order subspace, we take a low-rank approximation (Babaee & Sapsis 2016; Ramezanian, Nouri & Babaee 2021) as

$$\mathbf{Q}'(t) \approx \mathbf{U}_r(t)\mathbf{Y}_r(t)^{\mathrm{T}}, \tag{2.4}$$

where

$$\mathbf{U}_r(t) \equiv [\mathbf{u}_1(t), \mathbf{u}_2(t), \ldots, \mathbf{u}_r(t)] \in \mathbb{R}^{n\times r} \tag{2.5}$$

is a set of r time-dependent orthonormal basis vectors, and

$$\mathbf{Y}_r(t) \equiv [\mathbf{y}_1(t), \mathbf{y}_2(t), \ldots, \mathbf{y}_r(t)] \in \mathbb{R}^{d\times r} \tag{2.6}$$

is the reduced-order coefficient matrix. The full-order perturbation dynamics can be approximated properly with an appropriate choice of r basis vectors and their coefficients.

To derive the evolution equations for $\mathbf{U}_r(t)$ and $\mathbf{Y}_r(t)$, we trace the perturbation dynamics by substituting (2.4) into the linearized equation (2.3):

$$\frac{\mathrm{d}\left(\mathbf{U}_r\mathbf{Y}_r^{\mathrm{T}}\right)}{\mathrm{d}t} = \mathbf{U}_r\frac{\mathrm{d}\mathbf{Y}_r^{\mathrm{T}}}{\mathrm{d}t} + \frac{\mathrm{d}\mathbf{U}_r}{\mathrm{d}t}\mathbf{Y}_r^{\mathrm{T}} = \mathbf{L}\mathbf{U}_r\mathbf{Y}_r^{\mathrm{T}}. \tag{2.7}$$

Strictly speaking, $d(\mathbf{U}_r\mathbf{Y}_r^{\mathrm{T}})/\mathrm{d}t \neq \mathbf{L}\mathbf{U}_r\mathbf{Y}_r^{\mathrm{T}}$ due to the OTD low-rank approximation error. The evolution equations for $\mathbf{U}_r(t)$ and $\mathbf{Y}_r(t)$ can be obtained via a variational principle

according to Donello *et al.* (2022), which involves minimizing the residual

$$F\left(\frac{\mathrm{d}\mathbf{Y}_r}{\mathrm{d}t}, \frac{\mathrm{d}\mathbf{U}_r}{\mathrm{d}t}\right) = \left\| \mathbf{U}_r \frac{\mathrm{d}\mathbf{Y}_r^{\mathrm{T}}}{\mathrm{d}t} + \frac{\mathrm{d}\mathbf{U}_r}{\mathrm{d}t}\mathbf{Y}_r^{\mathrm{T}} - \mathbf{L}\mathbf{U}_r\mathbf{Y}_r^{\mathrm{T}} \right\|_F, \tag{2.8}$$

subject to the orthonormality constraints of OTD modes. In (2.8), $\|\cdot\|_F$ is the matrix Frobenius norm. The first-order optimality conditions of the above minimization principle yield the OTD evolution equations. The individual evolution equations for $\mathbf{U}_r$ and $\mathbf{Y}_r$ can alternatively be found via the Galerkin projection of (2.7) onto $\mathbf{U}_r$ and $\mathbf{Y}_r$ and enforcing the orthonormality condition of the time-dependent modes $\mathbf{U}_r^{\mathrm{T}}\mathbf{U}_r = \mathbf{I}$. Taking the time derivative of the orthonormality condition leads to

$$\mathbf{U}_r^{\mathrm{T}}\frac{\mathrm{d}\mathbf{U}_r}{\mathrm{d}t} + \frac{\mathrm{d}\mathbf{U}_r^{\mathrm{T}}}{\mathrm{d}t}\mathbf{U}_r = \mathbf{0}, \tag{2.9}$$

where we, henceforth, denote $\boldsymbol{\Phi} = \mathbf{U}_r^{\mathrm{T}}\mathrm{d}\mathbf{U}_r/\mathrm{d}t \in \mathbb{R}^{r\times r}$. In order to satisfy (2.9), $\boldsymbol{\Phi}$ needs to be a skew-symmetric matrix, i.e. $\boldsymbol{\Phi}^{\mathrm{T}} = -\boldsymbol{\Phi}$. The evolution equation for $\mathbf{Y}_r(t)$ can be found via projecting (2.7) onto $\mathbf{U}_r$. This is accomplished by multiplying both sides of that equation with $\mathbf{U}_r^{\mathrm{T}}$ from the left-hand side, which yields

$$\frac{\mathrm{d}\mathbf{Y}_r^{\mathrm{T}}}{\mathrm{d}t} = \left(\mathbf{U}_r^{\mathrm{T}}\mathbf{L}\mathbf{U}_r - \boldsymbol{\Phi}\right)\mathbf{Y}_r^{\mathrm{T}}, \tag{2.10}$$

where the orthonormality constraints, $\mathbf{U}_r^{\mathrm{T}}\mathbf{U}_r = \mathbf{I}$ and $\boldsymbol{\Phi} = \mathbf{U}_r^{\mathrm{T}}d\mathbf{U}_r/\mathrm{d}t$ are utilized. Similarly, the evolution equation for $\mathbf{U}_r(t)$ can be found projecting (2.7) onto $\mathbf{Y}_r$, which can be performed by multiplying that equation onto $\mathbf{Y}_r$ from the right-hand side. This results in

$$\frac{\mathrm{d}\mathbf{U}_r}{\mathrm{d}t} = \mathbf{L}\mathbf{U}_r - \mathbf{U}_r\left(\mathbf{U}_r^{\mathrm{T}}\mathbf{L}\mathbf{U}_r - \boldsymbol{\Phi}\right), \tag{2.11}$$

where (2.10) is utilized for $\mathrm{d}\mathbf{Y}_r^{\mathrm{T}}/\mathrm{d}t$ and the two sides of the equations are multiplied by $(\mathbf{Y}_r^{\mathrm{T}}\mathbf{Y}_r)^{-1}$. With these equations, we can evolve the time-dependent basis and the coefficient matrix given the time-varying linear operator $\mathbf{L}(t)$ and the initial conditions.

To further simplify (2.11) and (2.10), we can choose $\boldsymbol{\Phi} = \mathbf{0}$. The choice of the skew-symmetric matrix $\boldsymbol{\Phi}$ is not unique. With different choices of $\boldsymbol{\Phi}$, it can be proven that one OTD subspace is equivalent to another OTD subspace after being rotated by an orthogonal rotation matrix (Babaee & Sapsis 2016; Blanchard & Sapsis 2019*a*). When we choose a simple choice of $\boldsymbol{\Phi} = \mathbf{0}$, we have

$$\frac{\mathrm{d}\mathbf{U}_r}{\mathrm{d}t} = \left(\mathbf{I} - \mathbf{U}_r\mathbf{U}_r^{\mathrm{T}}\right)\mathbf{L}\mathbf{U}_r, \tag{2.12}$$

where $\mathbf{I} - \mathbf{U}_r\mathbf{U}_r^{\mathrm{T}}$ is the orthogonal projector onto the complement of subspace $\mathbf{U}_r$ (Donello *et al.* 2022). In this case, we arrive at the closed form of OTD evolution equations of

$$\frac{\mathrm{d}\mathbf{U}_r}{\mathrm{d}t} = \mathbf{L}\mathbf{U}_r - \mathbf{U}_r\left(\mathbf{U}_r^{\mathrm{T}}\mathbf{L}\mathbf{U}_r\right) \tag{2.13}$$

and

$$\frac{\mathrm{d}\mathbf{Y}_r^{\mathrm{T}}}{\mathrm{d}t} = \left(\mathbf{U}_r^{\mathrm{T}}\mathbf{L}\mathbf{U}_r\right)\mathbf{Y}_r^{\mathrm{T}}. \tag{2.14}$$

Based on the above time-dependent equations, we can evolve $\mathbf{U}_r(t)$ and $\mathbf{Y}_r(t)^{\mathrm{T}}$ given the initial conditions $\mathbf{U}_r(t_0)$ and $\mathbf{Y}_r(t_0)^{\mathrm{T}}$. Here, the choice of initial condition is also not

unique. However, the time-dependent modes from two different initial conditions span the same OTD subspace when one initial condition can be transformed into another one (Babaee *et al.* 2017).

The variational principle introduced in this work differs slightly from the minimization problem presented in Babaee & Sapsis (2016), though the resulting OTD evolution equations are identical. Since the evolution equation for $\mathbf{U}_r$ is independent of $\mathbf{Y}_r$, as is evident from (2.13) and (2.14), it is possible to formulate a variational principle with respect to $\mathrm{d}\mathbf{U}_r/\mathrm{d}t$, as shown in Babaee & Sapsis (2016) and obtain an evolution equation for $\mathbf{U}_r$. The evolution equation for $\mathbf{Y}_r^{\mathrm{T}}$ can be derived by projecting the full-order model of (2.2) onto $\mathbf{U}_r$. However, in the variational principle presented in (2.8), both $\mathrm{d}\mathbf{U}_r/\mathrm{d}t$ and $\mathrm{d}\mathbf{Y}_r/\mathrm{d}t$ are control variables and minimizing the functional in (2.8) yields the evolution equations for $\mathbf{U}_r$ and $\mathbf{Y}_r$. The variational principle presented in this work has the advantage of having a simple interpretation. The matrix $\mathbf{U}_r\mathbf{Y}_r^{\mathrm{T}}$ is a low-rank approximation of $\mathbf{Q}'$ with $\mathbf{U}_r$ and $\mathbf{Y}_r$ evolving to minimize the residual due to the low-rank approximation error.

In the above formulation, the time-dependent modes are correlated with each other. We can perform a rotation so that these modes are independent and ranked by their importance. To this end, let us consider a correlation matrix $\mathbf{C}(t) = \mathbf{Y}_r^{\mathrm{T}}(t)\mathbf{Y}_r(t) \in \mathbb{R}^{r\times r}$. The eigenvalue decomposition of this correlation matrix $\mathbf{C}(t)$ yields

$$\mathbf{C}(t)\mathbf{R}(t) = \mathbf{R}(t)\boldsymbol{\Lambda}(t), \tag{2.15}$$

where $\boldsymbol{\Lambda}(t) \equiv \mathrm{diag}(\lambda_1(t), \lambda_2(t), \ldots, \lambda_r(t))$ holds the set of eigenvalues and $\mathbf{R}(t) \in \mathbb{R}^{r\times r}$ is composed of the corresponding eigenvectors of $\mathbf{C}(t)$. Since $\mathbf{C}(t)$ is a symmetric positive matrix, $\mathbf{R}(t)$ is an orthonormal matrix and $\boldsymbol{\Lambda}(t)$ has all non-negative eigenvalues of $\lambda_1 \geq \lambda_2 \geq \cdots \geq \lambda_r$. Here, $\mathbf{C}(t)$ is generally a full matrix, which indicates that the coefficients are correlated.

A linear mapping from the correlated coefficients $\mathbf{Y}_r(t)$ to the uncorrelated coefficient matrix $\hat{\mathbf{Y}}_r(t)\boldsymbol{\Sigma}_r(t)$ can be found using the fact that the perturbations $\mathbf{U}_r\mathbf{Y}_r^{\mathrm{T}}$ can be decomposed through a singular value decomposition $\hat{\mathbf{U}}_r(t)\boldsymbol{\Sigma}_r(t)\hat{\mathbf{Y}}_r(t)^{\mathrm{T}}$. Such a mapping is realized by performing a matrix rotation and scaling

$$\hat{\mathbf{Y}}_r(t) = \mathbf{Y}_r(t)\mathbf{R}(t)\boldsymbol{\Sigma_r}^{-1}(t), \tag{2.16}$$

where $\boldsymbol{\Sigma}_r(t) \equiv \mathrm{diag}(\sigma_1(t), \sigma_2(t), \ldots, \sigma_r(t))$ holds singular values $\sigma_i(t) = \lambda_i(t)^{1/2}$. Thus, we now have the ranked spatial modes $\hat{\mathbf{U}}_r(t)$ based on the eigenvalues $\lambda_i(t)$:

$$\hat{\mathbf{U}}_r(t) = \mathbf{U}_r(t)\mathbf{R}(t). \tag{2.17}$$

We will, henceforth, refer to this ranked time-dependent modes $\hat{\mathbf{U}}_r(t)$ as the OTD modes. Since the leading mode possesses the largest singular value, the primary amplified structure of perturbations can be identified from the leading time-dependent mode. As an illustrative example, we show the OTD modes of three-dimensional Rössler system in figure 1. The two time-evolving vectors indicate the two dominant amplification directions of the perturbations.

One of the utilities of the OTD analysis is that it reveals the most amplified initial perturbation and the corresponding instantaneous amplification factor. The first singular vector and singular value of the OTD low-rank approximation contain information about the optimal perturbation. In particular, the most amplified perturbation is represented as $\mathbf{q}'_{*_1}(t) = \sigma_1(t)\hat{\mathbf{u}}_1(t)$ and the optimal initial perturbation that leads to the maximum amplification at time t is obtained via

$$\mathbf{q}'_{0_1}(t) = \hat{\mathbf{U}}_r(t_0)\boldsymbol{\Sigma}_r(t_0)\hat{\mathbf{Y}}_r(t_0)^{\mathrm{T}}\hat{\mathbf{y}}_1(t). \tag{2.18}$$

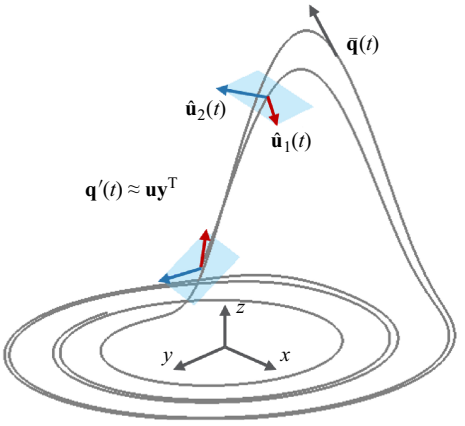

Figure 1. The evolution of the base flow $\bar{\mathbf{q}}(t)$ and the OTD modes $\mathbf{u}_i(t)$ for an example of the Rössler system. The perturbation $\mathbf{q}'(t)$ is captured by the product of OTD modes $\mathbf{u}(t)$ and their coefficients $\mathbf{y}(t)$.

The amplitude of the optimal perturbation is $\|\mathbf{q}'_{*_1}(t)\|_2 = \|\sigma_1(t)\hat{\mathbf{u}}_1(t)\|_2 = \sigma_1(t)$, since $\|\hat{\mathbf{u}}_1(t)\|_2 = 1$. The optimal initial perturbation is also time-dependent as evident from (2.18). That is, for each choice of t, a different optimal perturbation condition achieves the maximum amplification at time t and as time evolves, the optimal initial perturbation $\mathbf{q}'_{0_1}(t)$ varies smoothly. The optimal initial perturbation is confined to the space spanned by the columns of $\hat{\mathbf{U}}_r(t_0)\boldsymbol{\Sigma}_r(t_0)\hat{\mathbf{Y}}_r^{\mathrm{T}}(t_0)$. To obtain the maximum energy amplification, denoted as $g_1(t)$, the amplitude of the perturbation should be normalized with respect to the amplitude of the initial perturbation

$$g_1(t) \equiv \frac{\|\mathbf{q}'_{*_1}(t)\|^2}{\|\mathbf{q}'_{0_1}(t)\|^2} = \frac{\sigma_1^2(t)}{\|\mathbf{q}'_{0_1}(t)\|^2}. \tag{2.19}$$

Similarly, the higher-order suboptimal initial perturbations are

$$\mathbf{q}'_{0_i}(t) = \hat{\mathbf{U}}_r(t_0)\boldsymbol{\Sigma}_r(t_0)\hat{\mathbf{Y}}_r(t_0)^{\mathrm{T}}\hat{\mathbf{y}}_i(t), \quad i = 2, 3, \ldots, r. \tag{2.20}$$

The corresponding amplified perturbations are $\mathbf{q}'_{*_i}(t) = \sigma_i(t)\hat{\mathbf{u}}_i(t)$ for $i = 2, 3, \ldots, r$. Therefore, the levels of energy amplification $g_i(t)$ are found to be

$$g_i(t) \equiv \frac{\|\mathbf{q}'_{*_i}(t)\|^2}{\|\mathbf{q}'_{0_i}(t)\|^2} = \frac{\sigma_i^2(t)}{\|\mathbf{q}'_{0_i}(t)\|^2}, \quad i = 2, 3, \ldots, r. \tag{2.21}$$

For each OTD mode $\hat{\mathbf{U}}_i$, $g_1(t)$ is the maximum possible amplification of the perturbation energy that can occur in the fluid system over a given time horizon. The higher-order energy amplification $g_i(t)$, $i > 1$, may also capture important growth. Analysing the higher-order energy amplifications provides a supplemental understanding of the transient dynamics of the fluid system. Each singular value $\sigma_i(t)$ indicates the magnitude of each OTD mode, as shown in the SVD form of low-rank approximation of perturbations $\mathbf{Q}'(t) \approx \hat{\mathbf{U}}_r(t)\boldsymbol{\Sigma}_r(t)\hat{\mathbf{Y}}_r(t)^{\mathrm{T}}$. On the other hand, $g_i(t)$ is a direct indicator of how much energy is amplified for each OTD mode with respect to the initial perturbation energy.

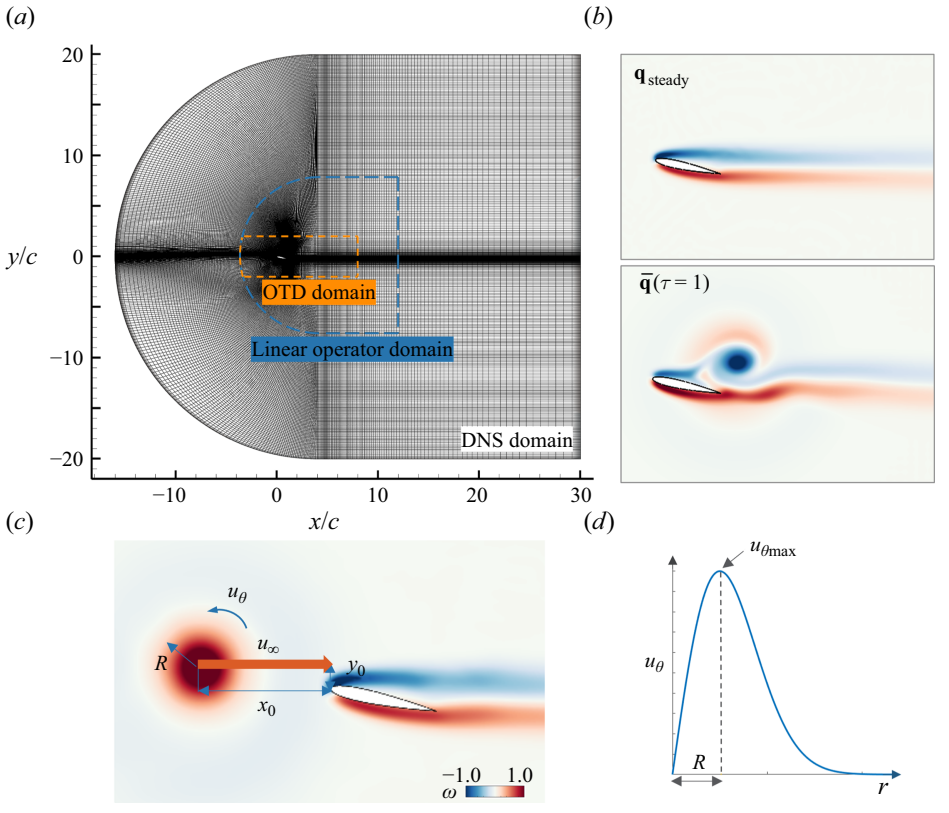

Figure 2. (*a*) Computational domains of DNS, linear operator and OTD mode analysis for vortex–airfoil interaction problem. (*b*) Vorticity fields of steady state (without vortex gust) and time-varying base state at $\tau = 1$. (*c*) Parameters of vortex–airfoil interaction problem. (*d*) Velocity profile of the vortex gust.

3. Model problem

3.1. *Problem set-up*

The OTD modes identify the transient amplification of a time-varying flow. With strong vortex–airfoil interactions exhibiting violent transient flow features, OTD mode analysis can be useful for capturing the perturbation dynamics. We study the transient amplifications of the complex interactions between a vortical gust and the NACA 0012 airfoil, as shown in figure 2. The base flow considered in OTD mode analysis is the flow disturbed by a vortex gust. Direct numerical simulations (DNS) of flows with and without a gust vortex-impingement are performed with the compressible flow solver CharLES (Khalighi *et al.* 2011*a*,*b*; Bres *et al.* 2017). Before interacting with a vortex gust, the two-dimensional flow is steady over an airfoil at an angle of attack of 12° for a chord-based Reynolds number $Re \equiv u_\infty c/\nu_\infty = 400$ and Mach number $M_\infty \equiv u_\infty/a_\infty = 0.1$. Here, u_∞ is the free stream velocity, c is the chord length, ν_∞ is the kinematic viscosity and a_∞ is the free stream sonic speed. The DNS domain is shown in figure 2(*a*), and the steady-state vorticity field is presented in figure 2(*b*).

We validate the DNS model without a vortex gust by comparing the time-averaged lift $\overline{C_L}$ on a NACA0012 airfoil with previous studies (Liu *et al.* 2012; Kurtulus 2016; Di Ilio *et al.* 2018), as shown in figure 3(*a*). At $Re = 1000$, the $\overline{C_L}$ from our simulation agrees well with the references over various angles of attack. The $\overline{C_L}$ from $Re = 400$ is generally

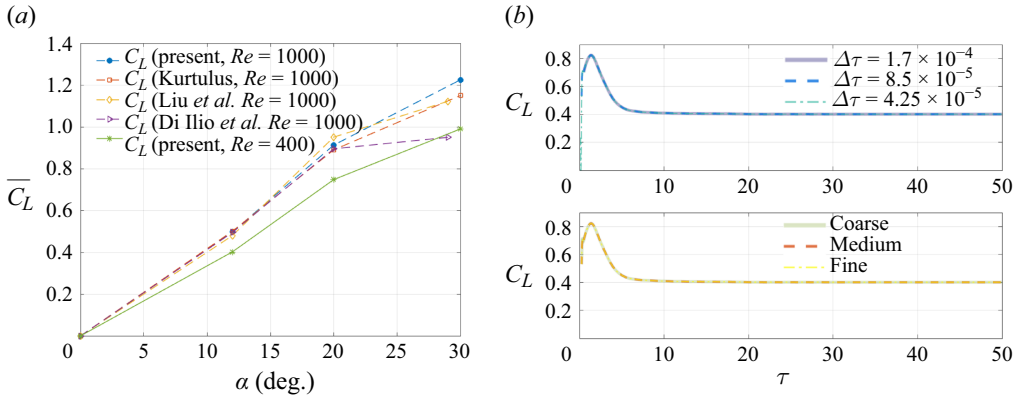

Figure 3. (*a*) Comparison of time-averaged lift coefficient between references and the present study over different angles of attack. (*b*) Temporal and spatial convergence of lift history for a NACA0012 airfoil at the angle of attack 12° and $Re = 400$.

lower than that from $Re = 1000$. In addition, time convergence and grid convergence are checked for our DNS results of the flow over a NACA0012 airfoil at $\alpha = 12°$ and $Re = 400$. The coarse, medium and fine meshes have grid points of 62 566, 74 046 and 194 012, respectively. Figure 3(*b*) shows that both time and grid convergence are achieved for the lift coefficient C_L over time. We chose the medium mesh and a Courant–Friedrichs–Lewy number of $a_\infty \Delta t/\Delta x < 1$ in our DNS. For the DNS of vortex–airfoil interactions, the results from the compressible solver CharLES has been compared with that from the incompressible solver Cliff. The lift coefficients match with each other with these two different solvers. In addition, time convergence and grid convergence are achieved for vortex–airfoil interactions.

A compressible Taylor vortex (Taylor 1918) is introduced upstream of the airfoil, whose angular velocity is given by

$$u_\theta = u_{\theta max} \frac{r}{R} \exp\left(\frac{1}{2} - \frac{r^2}{2R^2}\right), \tag{3.1}$$

where r is the radial coordinate from the vortex centre, R is the radius of the vortex, $u_{\theta max}$ is the maximum rotational velocity and (x_0, y_0) is the initial centre position of the vortex, as shown in figure 2(*c,d*). Here, the gust ratio is defined as

$$G \equiv \frac{u_{\theta max}}{u_\infty}. \tag{3.2}$$

For the current study, we consider $G \in \{-1, -0.5, 0.5, 1\}$ and $R/c = 0.5$. Disturbed flows with moderate ($G = \pm 0.5$) and strong ($G = \pm 1$) vortices are studied as representative examples of highly unsteady flow scenarios (Jones, Cetiner & Smith 2022; Zhong *et al.* 2023). As the initial condition of the simulations, vortices are introduced with their centres at $(x_0, y_0) = (-3c, 0)$. We define $\tau \equiv u_\infty t/c = 0$ as the time the centre of the vortex arrives at the leading edge of the airfoil placed at $(x_0, y_0) = (0, 0)$.

To start tracing the transient amplification of the fluid system with the optimal time-dependent modes, we need to choose an appropriate initial condition for the time-dependent modes and coefficient matrix. We take the initial guess of the perturbations $\mathbf{Q}'$ from the initial condition matrix

$$\mathbf{Q}'_0 \equiv [\mathbf{q}'_{\tau_a}, \mathbf{q}'_{\tau_a+\Delta\tau}, \ldots, \mathbf{q}'_{\tau_b}] \in \mathbb{R}^{n\times d}, \tag{3.3}$$

where $\mathbf{q}'_\tau \equiv \mathbf{q}_\tau - \mathbf{q}_{steady}$, and $\mathbf{q}_{steady}$ is the flow state matrix of steady state. When the airfoil is at an angle of attack of 12°, a steady flow is achieved in the absence of a vortical gust. For other flows without a steady state, $\mathbf{q}_{steady}$ can be approximated by taking the time average of the flow. The initial condition matrix is obtained by stacking d snapshots within $\tau \in [\tau_a, \tau_b]$ with a constant time interval $\Delta\tau$. Then, the initial OTD modes and their coefficients are chosen from the singular value decomposition of the initial condition matrix $\mathbf{Q}'_0$ as

$$\mathbf{Q}'_0 = \mathbf{U}\boldsymbol{\Sigma}\mathbf{V}^{\mathrm{T}} \approx \mathbf{U}_r(\tau_0)\mathbf{Y}_r^{\mathrm{T}}(\tau_0), \tag{3.4}$$

where $\mathbf{U} \in \mathbb{R}^{n\times d}$ and $\mathbf{V} \in \mathbb{R}^{d\times d}$ are the left and right singular vectors, respectively. By choosing the leading r vectors of $\mathbf{U}$ as the initial time-dependent modes $\mathbf{U}_r(\tau_0)$, the coefficient matrix $\mathbf{Y}_r(\tau_0)$ can be initialized as the first r vectors of $\mathbf{V}\boldsymbol{\Sigma}$. Here, the initial evolution moment is indicated with τ_0.

After obtaining the initial OTD modes and their coefficients, we use the fourth-order Runge–Kutta time-stepping method to solve the OTD evolution (2.13)–(2.14) with the time-dependent linear operator $\mathbf{L}(t)$. To reduce the computational cost, the unsteady base state $\bar{\mathbf{q}}(t)$ obtained from the DNS is interpolated into a smaller domain to extract the linear operator $\mathbf{L}(t)$ (Sun *et al.* 2017), as shown in figure 2(*a*). The Dirichlet boundary condition is applied to the far-field boundary and the airfoil, and the Neumann boundary condition is set as the outlet boundary condition. With these boundary conditions, we extract the linear operator $\mathbf{L}(t) \in \mathbb{R}^{n\times n}$ in a discrete form. Here, the degrees of the freedom of the discretized flow $n = 428\,370$. To further reduce the computational cost, we restrict the OTD domain as the linear operator domain overlapping with the rectangle $(x, y)/c \in [-4, 8] \times [-2, 2]$. As all OTD modal structures appear around the airfoil, changing the OTD domain size does not affect the OTD modes and their coefficients.

In the current study, the initial time for OTD analysis is chosen as $\tau_0 = -1$. The initial condition matrix is formulated by collecting a total of $d = 710$ flow state vectors from $[\tau_a, \tau_b] = [-1, -0.4]$, during which time the vortical gust advects from upstream of the airfoil towards the leading edge of the airfoil. The initial conditions are carefully selected before the vortex gust interacts with the airfoil. This choice is critical for analysing the response to upstream disturbances and enabling timely interventions to suppress the growth of perturbations during the vortex–airfoil interaction. We consider the overall OTD analysis over $\tau \in [-1, 1]$. Additional details on the initial modes are discussed in appendix A, and discussions on the optimal initial perturbation are presented in appendix B.

3.2. *Flow physics*

Vortex–airfoil interactions exhibit strong transient characteristics within a short time. Previous studies have shown that vortex–body interaction may involve both rapid distortion of the incident vorticity field and injection of vorticity from the surface of the body (Rockwell 1998; Eldredge & Jones 2019; Martínez-Muriel & Flores 2020; Qian, Wang & Gursul 2022; Fukami & Taira 2023). To inform our interpretation of the dominant OTD modes, we analyse the perturbation evolution during the vortex–airfoil interaction process. Here, we first analyse the dynamics of the unsteady base flows of the aforementioned four vortex–airfoil interaction cases. The time evolution of the vorticity fields and the aerodynamic forces of the vortex–airfoil interaction cases are presented in figure 4. The lift and drag coefficients are defined as $C_L = F_L/(0.5\rho u_\infty^2 c)$ and $C_D = F_D/(0.5\rho u_\infty^2 c)$, respectively, where F_L is the lift force and F_D is the drag force on the airfoil. Initially, the

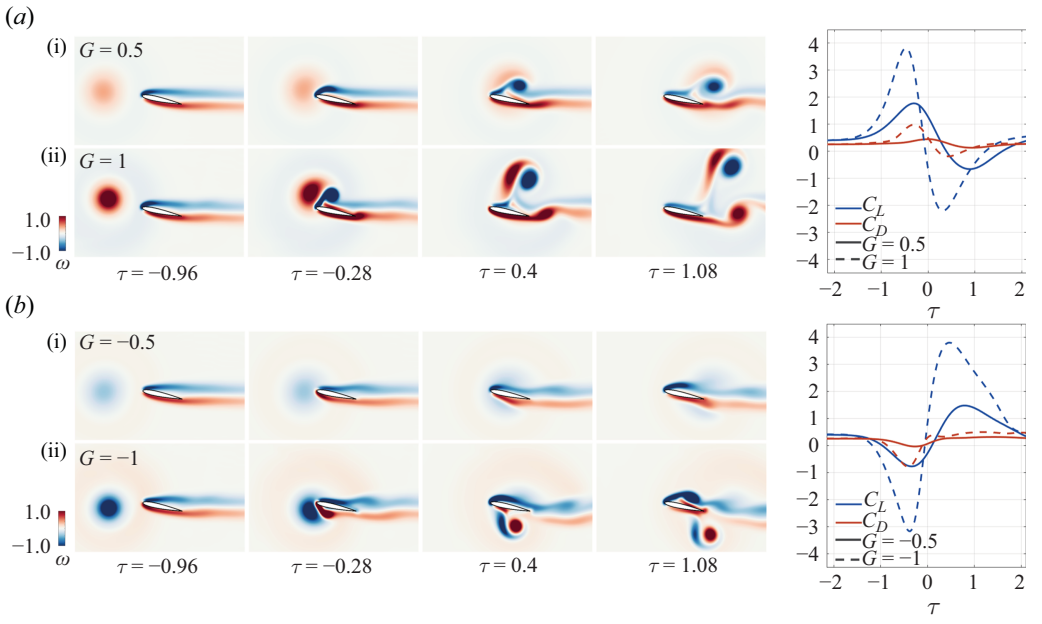

Figure 4. Vorticity fields and aerodynamic forces disturbed by (*a*) a positive and (*b*) a negative vortex gust.

vortical disturbance is introduced upstream of the wing. This vortex approaches the airfoil and produces large transient effects around the airfoil.

The dynamics of a positive (anticlockwise) vortex interacting with a NACA0012 airfoil is presented in figure 4(*a*). A positive vortex gust induces lift and drag force increase as it impinges on the leading edge of the airfoil. Shortly thereafter, the aerodynamic forces decrease once the centre of the vortex convects past the centre of the airfoil. When a moderate positive vortex ($G = 0.5$) first impinges on the airfoil, negative vorticity generated at the leading edge quickly rolls up into a leading-edge vortex (LEV) above the airfoil surface, as seen at $\tau = -0.28$. The increase of the negative circulation due to the growth of the LEV results in a lift augmentation on the airfoil (Dickinson & Götz 1993; Eldredge & Jones 2019). After the LEV detaches from the LEV sheet around $\tau = 1$, the vortex advects into the wake. For a strong positive vortex ($G = 1$) shown in figure 4(*a*), the interactions between the vortex and the airfoil generate a large LEV forming a vortex pair with the gust vortex, which moves far away from the airfoil body. Such a strong interaction produces four times larger lift and drag fluctuations compared with a moderate vortex–airfoil interaction with $G = 0.5$. In addition, a trailing-edge vortex is produced as the centre of the strong vortex passes over the wing around $\tau = 1$. The shedding of the trailing-edge vortex is not seen in the moderate positive vortex–airfoil interaction of $G = 0.5$, indicating that the $G = 1$ case has more drastic transient effects on wakes around the airfoil.

A negative (clockwise) vortex gust induces different effects on wake dynamics and aerodynamic performance compared with a positive vortex gust. For a moderate negative vortex case ($G = -0.5$) shown in figure 4 (*b* i), the gust vortex does not cause large-scale flow separations as it convects around the airfoil, but imposes lift variation of approximately five times the steady-state lift. For a strong negative vortex gust of $G = -1$, such a disturbance induces massive flow separation on both sides of the wing, as shown in figure 4 (*b* ii). A large positive vortex is formed from the pressure-side roll-up around $\tau = 0.4$. When the disturbance moves away from the airfoil around $\tau = 1$, the remaining

effect of the gust vortex is still sufficiently strong to disturb the flow on the suction side of the airfoil, producing a secondary LEV. Moreover, the airfoil experiences lift reduction and augmentation that are approximately 10 times larger than the steady-state lift when interacting with a negative vortex gust.

From these cases, we identify different transient features of the disturbed airfoil wakes impinged by a gust vortex. We consider these vortex–airfoil interaction cases as the unsteady base flows and examine the perturbation dynamics of each of these base flows using the OTD mode analysis below.

4. The OTD mode analysis

Given the time-varying base flows studied in § 3.2, the OTD mode analysis is performed to reveal the transient flow structures that may be amplified throughout the vortex–airfoil interactions. The OTD modes reveal regions where perturbations can undergo amplification with respect to the time-varying base flow. Four interaction scenarios involving a moderate positive vortex ($G = 0.5$), a strong positive vortex ($G = 1$), a moderate negative vortex ($G = -0.5$) and a strong negative vortex ($G = -1$) are examined. Verification of numerical calculations for the OTD modes is provided in appendix B.

Let us first examine the case of moderate positive vortex ($G = 0.5$), which advects over the airfoil and induces a new vortex roll-up above the airfoil. Given the transient variations of the unsteady base flow, we now investigate when and where perturbations can possibly be amplified through the lens of the OTD modes. We present the leading three time-dependent modes in the order of their singular values $\sigma_i(\tau)$. The vorticity fields and the top three time-dependent vorticity modes over time are shown in figure 5(*a*). The temporal evolution of the leading three singular values is depicted in figure 5(*b*), and the leading three levels of energy amplification are shown in figure 5(*c*).

Around $\tau = -0.5$, the vortical gust advects towards the leading edge of the airfoil. The primary amplified region, highlighted by dominant spatial modes, appears around the top boundary layer near the leading edge of the airfoil. At the same time, the secondary amplified region emerges to coincide with the core of the vortical disturbance, shown upstream of the leading three OTD modes. Additionally, streamwise oscillations in the model structures appear for the higher-order modes 2 and 3. Therefore, during the period when the vortex approaches the airfoil, the primary amplified structure stems from the boundary layer near the leading edge of the airfoil and the subdominant sensitive regions correlate with the advection of the baseline vortical disturbance.

After the vortical gust impinges on the airfoil, the boundary layer separates and rolls up into an LEV. Around $\tau = 0$, modes 1 and 2 identify the amplification of perturbations colocated and corotating with the LEV, as indicated above the suction side of the airfoil in figure 5(*a*). During the LEV formation, perturbations can experience maximum amplification along the core of the LEV. As the centre of the vortical disturbance nears the half-chord position around the airfoil at $\tau = 0.5$, the LEV grows and moves towards the trailing edge of the airfoil. During this time, the most amplified region extends and shifts in the streamwise direction while rotating with the core of the LEV. By $\tau = 1$, the LEV in the base flow has detached from the airfoil. During this time, the primary OTD mode still follows the advection and rotation of the LEV, while the wake region behind the trailing edge of the airfoil becomes increasingly important due to the trailing-edge vortex sheet roll-up. This shows the transition of the most amplified flow structure from the LEV to the wake behind the airfoil.

By examining the singular values and energy amplifications, we identify the evolution of each OTD mode over time. Temporal changes of the corresponding singular values

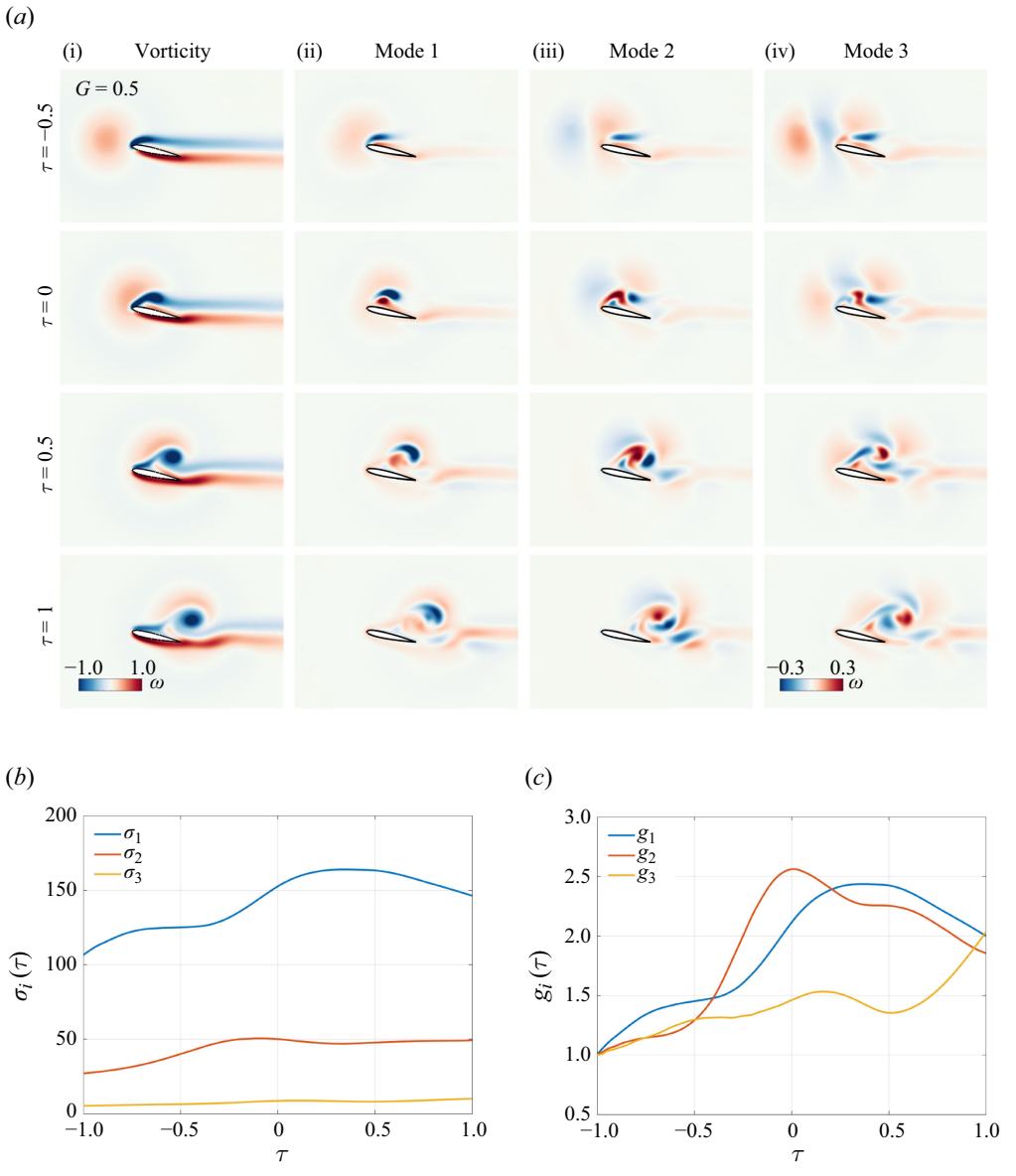

Figure 5. (*a*) Vorticity fields of the time-varying base flow and the top three OTD vorticity modes, (*b*) the leading three singular values and (*c*) the leading three energy amplifications for $G = 0.5$.

and energy amplifications $g_i(t)$ are presented in figures 5(*b*) and 5(*c*). The first OTD mode aligns with the most amplified direction during the evolution, associated with a large singular value of $O(100)$. In figure 5(*c*), the maximum possible energy amplification $g_1(t)$ and the suboptimal energy amplifications $g_2(t)$ and $g_3(t)$ have an increasing trend before $\tau = 0$. The increasing energy amplifications indicate that the perturbations can undergo a large transient growth as the LEV is forming. After the LEV detaches from the airfoil body around $\tau = 0.5$, the optimal and suboptimal energy amplifications become twice their initial values, which uncovers that the perturbations can experience large amplification in the trailing-edge wakes. Later, at $\tau = 1$, the third OTD mode shows

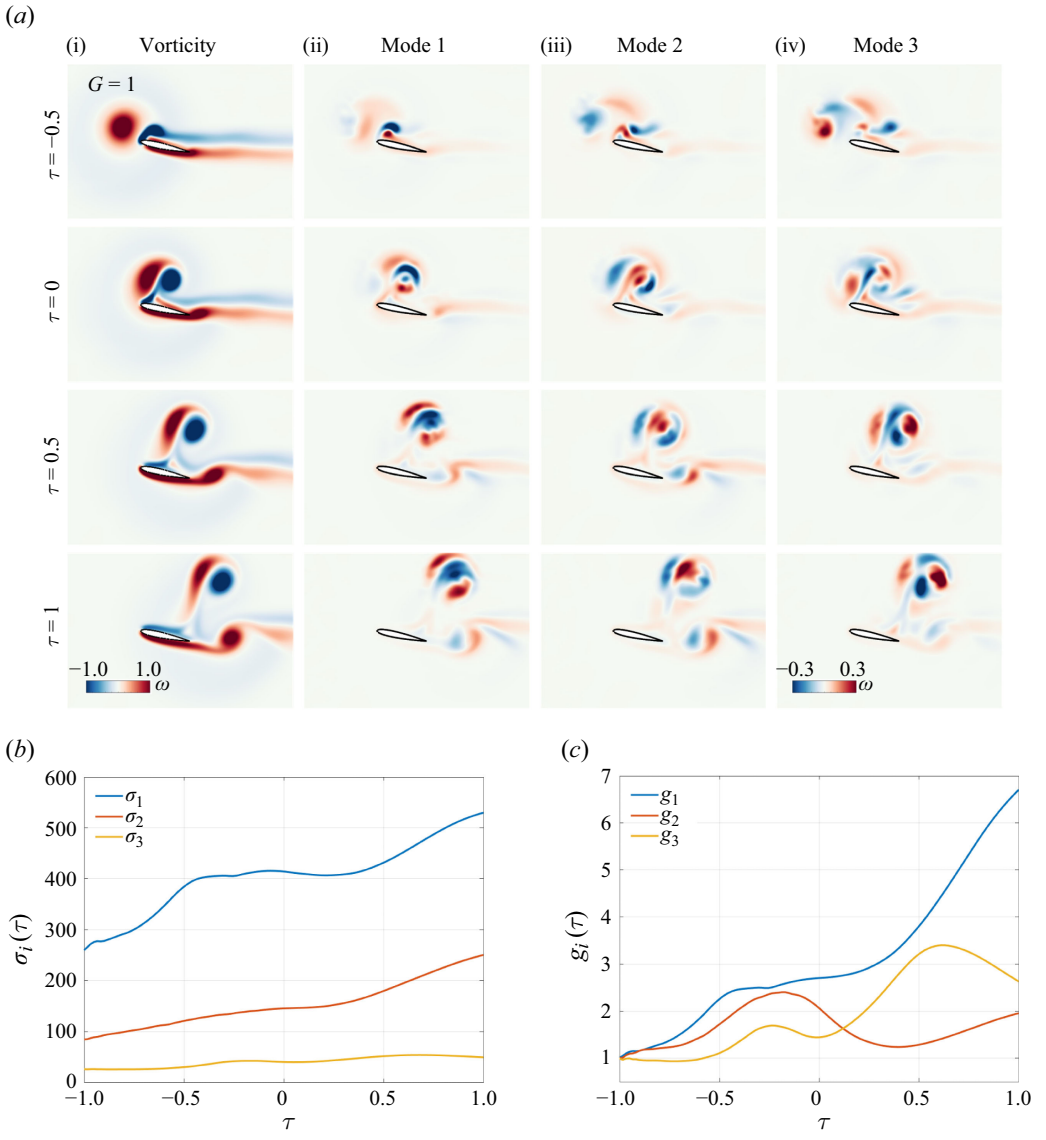

Figure 6. (*a*) Vorticity fields of the time-varying base flow and the top three OTD vorticity modes, (*b*) the leading three singular values and (c) the leading three energy amplifications for $G = 1$.

growth in energy. This third OTD mode exhibits finer flow structures, indicative of its role in capturing more localized and higher-frequency dynamics within the flow field. As the interaction progresses, the observed increase in the energy growth of this mode suggests an amplification of these finer structures, likely driven by the development of small-scale instabilities and the transfer of energy from larger to smaller scales within the vortex–airfoil interaction.

Now, let us consider the impact of vortex strength on the transient amplification of perturbations. In the case of a disturbed flow with a strong positive vortical gust of $G = 1$, the vorticity field undergoes prominent transient fluctuations, as shown in figure 6(*ai*). The dominant three spatial time-dependent modes are also presented. Around $\tau = -0.5$, the strong vortex induces drastic deformation of the vortex sheet around the leading edge

of the airfoil. During this time, the primary and secondary modes exhibit substantial amplification potential of perturbations in a localized region concentrated on the core of the vortex roll-up. Shortly after $\tau = 0$, the strong dipole (vortex pair) forms over the airfoil surface. The core of the negative LEV emerges as the most amplified region shown in modes 1 and 2. Mode 3 highlights a thin region between the positive vortex and the negative vortex in the LEV pair, suggesting that the stretching of vortex filaments within the LEV can lead to the growth of perturbations.

Later, when the vortex pair detaches from the airfoil after $\tau = 0.5$, all three dominant OTD modes identify the vortex pair as the most amplified flow structure. Concurrently, a small positive vortical structure in the base flow emerges at the trailing edge around $\tau = 0.5$. The amplified region behind the trailing edge suggests that a secondary amplification of the perturbations is associated with the formation of a trailing-edge vortex. From the analysis of the OTD modes over time, we find that the most amplified flow structures follow the vortices induced during the interaction between the strong vortical gust and the airfoil. The LEV pair, being a focal point of energy concentration, coincides with the maximum amplification regions of the OTD modes. The dominant singular values and the energy amplifications over time are shown in figure 6(*b–c*). Across all three modes, singular values exhibit a steady increase from $\tau = -1$ to 1. The optimal energy amplification is approximately seven times its initial value, revealing that perturbations can be continuously amplified during the interaction between the vortex and the wing. The second and third energy growths are non-monotonic, suggesting that the higher-order modes have different temporal growth rates compared with the first mode.

In contrast, when encountering a negative vortical gust, the dynamics of perturbations differ from those cases of positive vortex–airfoil interactions. We employ OTD mode analysis for the unsteady base flow concerning interactions between an airfoil and a moderate vortical gust ($G = -0.5$). Despite inducing significant lift and drag fluctuations on the airfoil, a moderate negative gust does not lead to large vortex shedding upon impingement, as visualized in figure 7(*a*). Regarding the perturbation amplification, the primary OTD mode only exhibits a gradual change in the most amplified flow structures. The amplified regions identified by mode 1 are associated with the deformation of the wakes from $\tau = -0.5$ to 1.

The time evolution of the amplified regions in modes 2 and 3 exhibits different perturbation dynamics from mode 1. Before $\tau = -0.5$, modes 2 and 3 do not exhibit any prominent features in spatially sensitive areas. As the moderate negative vortex interacts with the airfoil around $\tau = 0$, the boundary layer separates from the pressure side of the airfoil and becomes highlighted by OTD modes 2 and 3. Subsequently, as the vortical gust advects downstream after $\tau = 0.5$, a compact amplified area from the bottom side vortex sheet roll-up is captured in the second and third modes. This result suggests that the second and third modes are more sensitive to localized disturbances and transient phenomena. This underscores the importance of higher-order modes in providing a comprehensive understanding of the vortex–airfoil interaction, particularly in capturing the nuanced flow features that govern the local perturbation behaviour.

The corresponding singular values and perturbation amplifications are shown in figure 7(*b–c*). The leading singular value $\sigma_1 = O(100)$ remains fairly flat during its evolution, corresponding to the gradual changes of the leading OTD mode. On the other hand, the secondary energy amplification $g_2(t)$ shows a spike around $\tau = -0.1$, as depicted in figure 7(*c*). The large energy amplification of mode 2 indicates that the perturbations can grow large when the bottom side vortex sheet starts to roll up. The ability of the second mode to detect and amplify during the onset of roll-up underscores its importance in tracking the timing of transient perturbation amplification. Eventually all

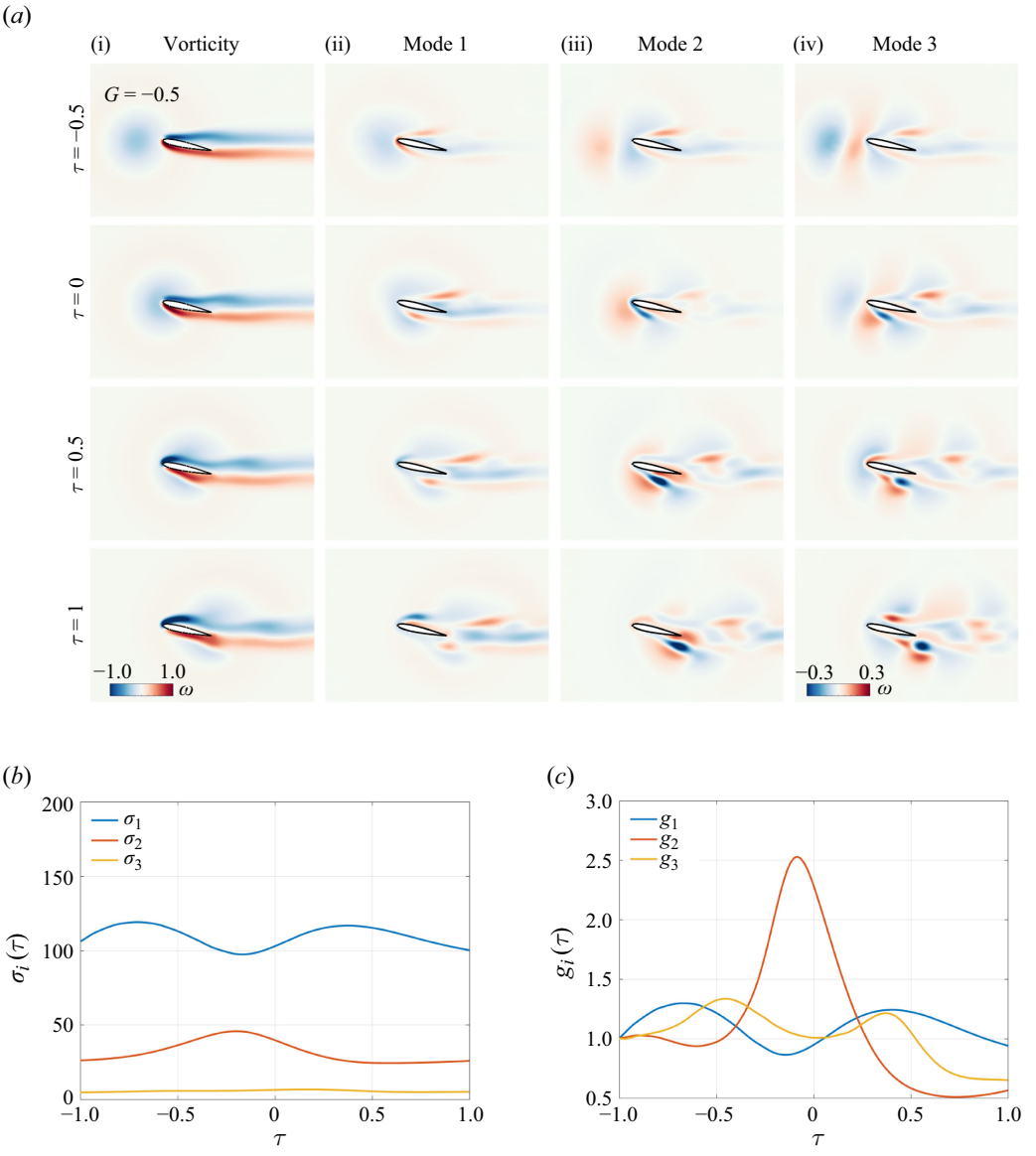

Figure 7. (*a*) Vorticity fields of the time-varying base flow and the top three OTD vorticity modes, (*b*) the leading three singular values and (*c*) the leading three energy amplifications for $G = -0.5$.

three energy amplifications become lower than 1 at $\tau = 1$, suggesting a loss of coherent structures and a decrease in the energy of the OTD modes.

Let us now consider the interactions between a strong negative vortical gust ($G = -1$) and an airfoil, which inherently include high levels of unsteadiness and nonlinearity. As visualized in figure 8(*a*), a large vortex pair is generated from the pressure side of the airfoil around $\tau = 0$ during the violent interaction. After the vortex pair detaches from the airfoil body around $\tau = 1$, a smaller LEV is generated from the vortex sheet roll-up on the suction side of the airfoil. The three dominant modes in general highlight the most amplified region following the large vortex pair below the airfoil, shown in figure 8(*a*). Modes 1–3 have similar modal structures with notable features about the positive vortex.

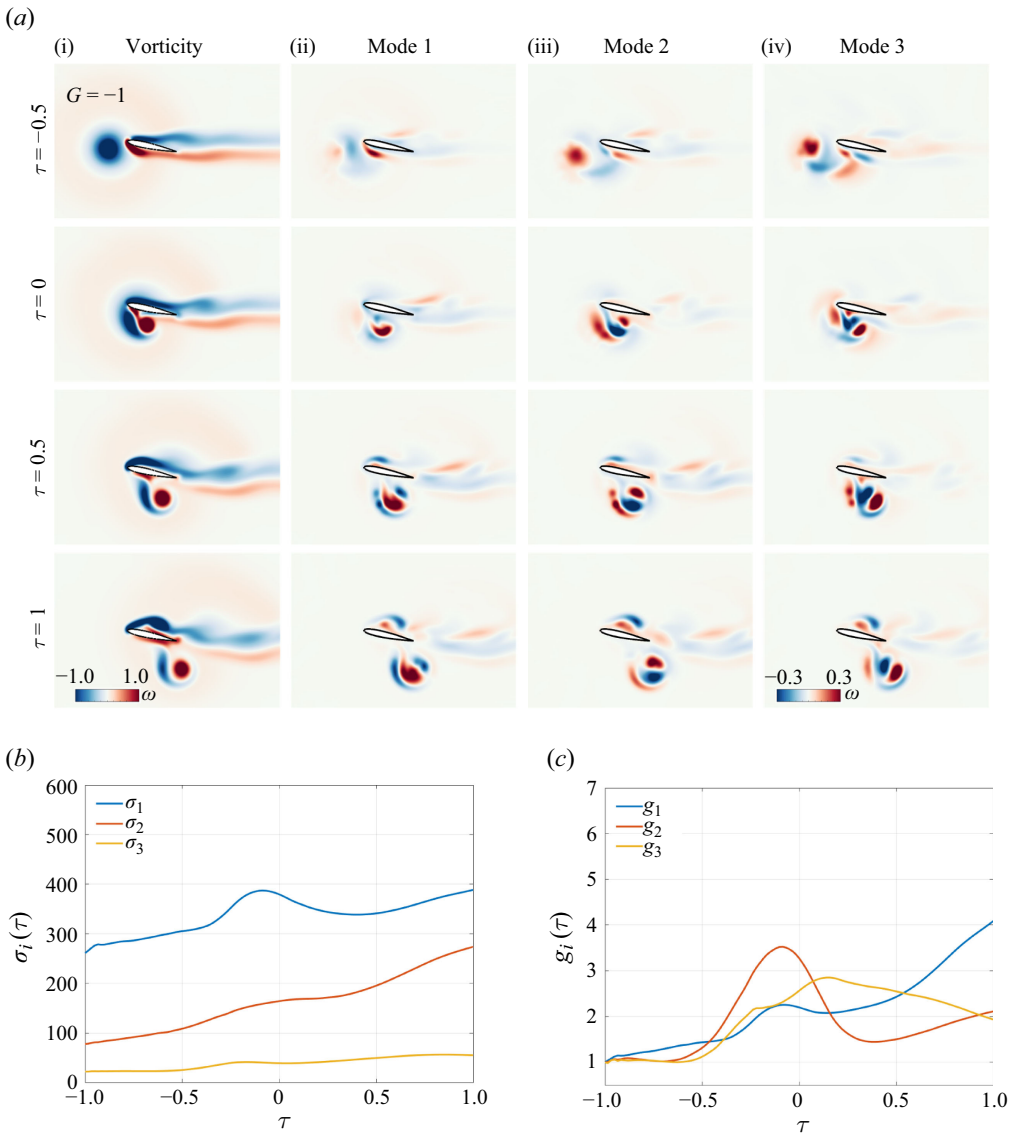

Figure 8. (*a*) Vorticity fields of the time-varying base flow and the top three OTD vorticity modes, (*b*) the leading three singular values and (*c*) the leading three energy amplifications for $G = -1$.

The most amplified structures coincide with the motion and rotation of the vortex pair that is generated around $\tau = 0$. In addition, a secondary sensitive region is found to be related to the subsequent vortex roll-up above the airfoil, as indicated by the emerging spatial structures about the LEV around $\tau = 1$.

In figure 8(*b,c*), the variations of the three leading singular values and energy amplifications show that the amplification of perturbations generally becomes larger over $-1 \leq \tau \leq 1$. In this case, the interaction between the strong negative vortex and the airfoil gives rise to a high level of perturbation amplifications. The suboptimal energy amplification $g_2(t)$ exhibits one peak around $\tau = -0.1$, as shown in the figure 8(*c*). During this time, both the positive and negative vorticity on the bottom side of the airfoil are

highlighted by OTD mode 2. This result suggests that the perturbations can be amplified both in the LEV and the strong disturbance vortex. Later when the LEV convects into the wake near the airfoil trailing edge, the optimal energy amplification $g_1(t)$ becomes four times its initial value during evolution, as presented in figure 8(c). The increasing trend of energy growth indicates a substantial amplification of perturbations.

The uncovering of optimal time-dependent modes offers valuable insights for understanding transient amplification in response to perturbations about unsteady flows. By leveraging the most amplified structures discovered by OTD mode analysis, we can pinpoint the most amplified regions subject to time-varying perturbations. For a moderate positive vortex–airfoil interaction case ($G = 0.5$), OTD modes unveil complex transitions of amplified flow structures from the LEV sheet to the forming LEV, with a secondary sensitive region as the wakes behind the airfoil. On the other hand, the leading amplified structures evolve slowly when the airfoil encounters a moderate negative vortical gust ($G = -0.5$). When the airflow is disturbed by a strong vortex ($G = \pm 1$), OTD modes expose a direct correlation between shedding vortex trajectory and transient amplification of perturbations.

The energy amplification of OTD modes provides valuable insights into the underlying dynamics that govern the evolution of perturbations. A monotonic increase in energy amplification, as seen in $g_1(t)$ ofthe $G = \pm 1$ cases, indicates a persistent instability mechanism. This mechanism for these two vortex–airfoil interactions is correlated with the high intensity of the vorticity of the primary shedding vortex. However, the region with the highest amplification is not always associated with the largest vorticity magnitude. For the example of $G = -0.5$, the highlighted modal structures of all three leading modes do not collapse on the leading edge of the airfoil where the highest vorticity magnitude is observed. Diverse transient behaviours are uncovered by the variations of energy amplification. For example, g_1 and g_2 exhibit rapid increases followed by decreases, as shown in figure 5. A rapid increase in energy amplification indicates a highly unstable region of the flow. The roll-up of the LEV for $G = 0.5$ corresponds to increasing energy amplifications. This region is prone to perturbations that can quickly amplify and lead to significant flow modifications. The subsequent decay suggests that the instability is transient, energy can be transferred downstream because of the wake formation.

The OTD mode analysis can be used to identify perturbation dynamics for more complex flows, such as extreme aerodynamic flows and turbulent flows. Capturing the coherent structures that are receptive to perturbations in a time-evolving manner is critical in understanding the unsteady flow physics. In addition, OTD mode analysis has the potential to guide flow control strategies. The OTD modes evolve dynamically, identifying when and where perturbations are most likely to grow. The OTD modes inform when the flow is most receptive to perturbations, suggesting that actuators or energy inputs (e.g. actuation via jets or local forcing) can be applied at the most effective moments to amplify (or suppress) instabilities. For example, for the $G = 0.5$ case, when the vortex is approaching the airfoil, the most amplified region is the leading edge of the airfoil. The control effects at this moment should focus on the local region around the leading edge. On the other hand, when the vortex convects to the trailing edge of the airfoil, the trailing edge can be amplified more compared with the leading edge. A different local forcing near the trailing edge will be more efficient than the leading edge at this specific moment.

5. Conclusions

Vortex–airfoil interactions involve strong transient features, which are difficult to characterize with classical methods that are founded on time-invariant or periodic flow.

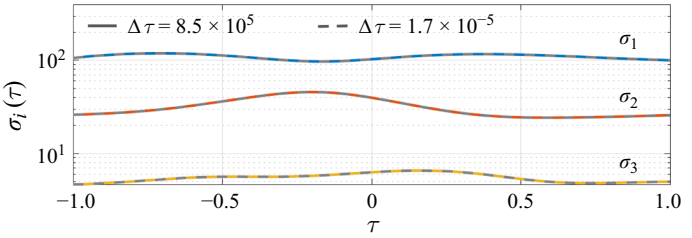

Figure 9. Time convergence on the top three singular values of moderate negative vortex–airfoil interaction.

In this study, OTD mode analysis was used to identify the most amplified flow structures of unsteady base flows of vortex–airfoil interactions. We considered four scenarios of vortex–airfoil interaction with a moderate positive vortex ($G = 0.5$), a strong positive vortex ($G = 1$), a moderate negative vortex ($G = -0.5$) and a strong negative vortex ($G = -1$). The OTD modes capture the most amplified regions subject to perturbations, and the singular value variations offer insights into the significance of the OTD modes. For the vortex–airfoil interaction of $G = 0.5$, the amplified region transitions from the LEV sheet to the evolving LEV. In addition, a secondary amplified flow structure near the trailing-edge wake is revealed by subdominant OTD modes. When a strong positive vortical gust ($G = 1$) interacts with an airfoil, perturbations are amplified following the advection and rotation of the LEV pair generated from the impingement of the strong vortical gust. For a moderate negative vortex disturbance ($G = -0.5$), the flowfield exhibits few dominant vortical structures, and thus, the dominant OTD mode follows the advection of the wakes around the airfoil and undergoes gradual changes over time. For the strong negative vortex–airfoil interaction of $G = -1$, the shedding vortex pair convecting from the pressure side of the airfoil surface is identified as the most amplified flow structure subject to perturbations. The findings through the OTD mode analysis for the present vortex–gust airfoil interactions provide insights into the transient amplification of perturbations in unsteady flight conditions and hold promising implications for diverse unsteady flow problems.

Acknowledgments. Y.Z. and K.T. acknowledge the support from the US Air Force Office of Scientific Research (grant no. FA 9550-21- 1-0178) and the US Department of Defense Vannevar Bush Faculty Fellowship (grant no. N 00014-22- 1-2798).

Declaration of interest. The authors report no conflict of interest.

Appendix A. Verification of OTD modes

The OTD modes are obtained by time-integrating the evolution (2.13). In this appendix, we briefly outline the checks performed to ensure the accuracy of the OTD modes. We first check the temporal convergence of the top three singular values, as shown in figure 9 for the case of $G = -0.5$. Using different time step sizes of $\Delta\tau = 8.5 \times 10^{-5}$ and 1.7×10^{-4}, the singular values from the two cases match well with each other over time. Therefore, we choose $\Delta\tau = 1.7 \times 10^{-4}$ as the default time step for finding the OTD modes.

Next, we examine the convergence on the number of OTD modes r. This is studied by comparing the singular values for different numbers of modes r. For brevity, we present only positive vortex–airfoil interaction cases in the following analyses. The negative vortex–airfoil interaction cases exhibit analogous results. As presented in figure 10 for positive gust cases, the top five singular values over time are shown for $r = 5$, 15 and 40. The solid lines represent the $r = 40$ cases, the dashed lines denote the $r = 15$ cases

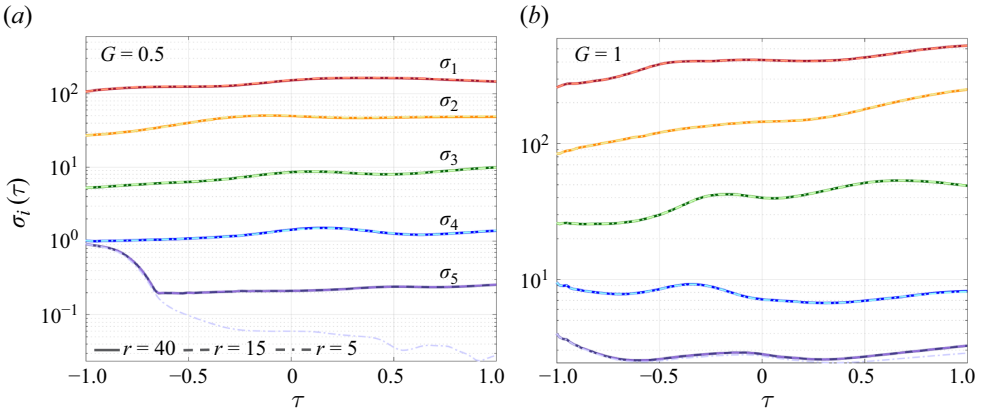

Figure 10. Convergence on the number of OTD modes for the top five singular values of four disturbed flow cases: (*a*) $G = 0.5$, (*b*) $G = 1$.

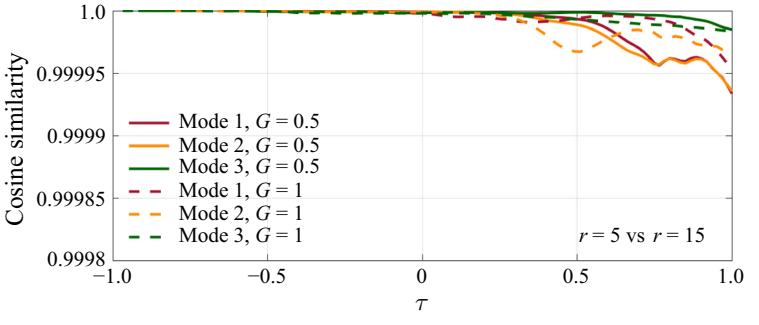

Figure 11. Cosine similarity of each of the three dominant modes between $r = 5$ and $r = 15$ of positive vortex–airfoil interaction cases.

and the dashed–dot lines are the $r = 5$ cases. In general, the leading three singular values of cases with different numbers of modes agree perfectly with each other. However, the lowest $r = 5$ cases have discrepancies in the fourth and fifth singular values compared with cases with a larger number of modes. Hence, we concluded that the singular values exhibit convergence with 15 modes for positive vortex–airfoil interaction cases.

The convergence check on the number of modes is also performed by comparing the cosine similarity between modes. Cosine similarity is defined as the inner product of two vectors, whose absolute value is in the range of [0, 1]. When the absolute cosine similarity approaches 1, it indicates that the two vectors are similar to each other. For convenience, we present the absolute value of the cosine similarity between OTD modes below. We examine the cosine similarity of the dominant three modes betweenthe $r = 5$ and 15 cases. Figures 11(*a*) and 11(*b*) show the vortex–airfoil interaction cases for positive vortices, respectively. Among the comparisons of positive vortex cases of $G = 0.5$ and 1, all three modes from the $r = 5$ cases achieve over 99.99 % cosine similarity with the corresponding modes from $r = 15$ cases. The high similarity levels demonstrate the high agreement of the leading three modes extracted from disturbed flow scenarios. With only $r = 5$ modes, the top three modes are as accurate as using 15 modes.

Now we investigate the influence of initial evolution time τ_0 on the OTD modes, the leading singular values converge while being insensitive to the choice of the OTD

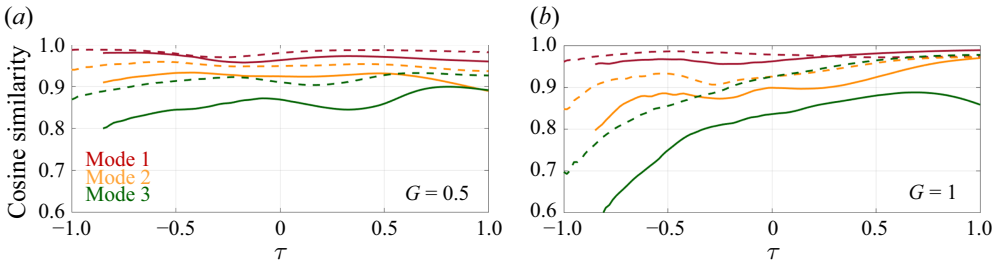

Figure 12. The influence of initial time for OTD evolution. For each of the leading three OTD modes, cosine similarity is checked between modes computed with initial time $\tau_0 = -0.85$ and -1 (solid lines), and between $\tau_0 = -1.12$ and -1 (dashed lines). The initial condition matrix is extracted from the flow state snapshots over $[\tau_a, \tau_b] \in [-1, -0.4]$.

initial condition time τ_0. Using the same initial condition matrix considering $[\tau_a, \tau_b] = [-1, -0.4]$, we integrate the initial OTD modes from different initial times of $\tau_0 = -1.12$, -1 and -0.85. The influence of different initial times on the evolution of the leading three modes is presented in figure 12. The solid lines indicate the comparison of each of the leading three modes computed with $\tau_0 = -0.85$ and -1, and the dashed lines are computed with $\tau_0 = -1.12$ and -1. In the case of $G = 0.5$, each of the three dominant modes with different initial evolution moments maintains over 80 % similarity throughout the entire time span. For the vortex–airfoil interaction cases of $G = 1$, however, the similarities start from relatively low values and increase afterward. This indicates that the observed dominant features converge to the same subset of OTD modes regardless of the initial evolution moments. Based on these results, we perform the OTD mode evolution from $\tau_0 = -1$, and the initial condition is given by $[\tau_a, \tau_b] = [-1, -0.4]$.

To show that the primary OTD mode shown earlier in figure 5 is not dependent on the initial condition, let us also consider random noise as the initial condition and evolve the OTD modes in time for the $G = 0.5$ case. We use 15 orthonormal random noise vectors as the initial OTD modes at $\tau = -1$.

As shown in the figure 13, the OTD mode 1 captures very similar structures to the case shown in the figure 5 when $\tau > 0$. The amplified region starts from the LEV sheet around $\tau = -0.5$, then evolves with the shedding of the LEV. Later around $\tau = 1$, the region after the trailing edge of the airfoil is highlighted as the most amplified region. On the other hand, OTD modes 2 and 3 are filled with random noises evolved from the initial condition. The noise structures get smoothed out as time increases, and vortical structures similar to OTD mode 1 are observed near the airfoil.

Compared with the initial modes, which are the singular vectors from the initial perturbation matrix, random noise as the initial condition yields a worse result in capturing the perturbation amplification. Although the OTD modes converge to the most amplified structures subject to perturbations, the convergence requires a large number of initial condition vectors. Therefore, we infer that a proper set of initial OTD modes can be selected from the SVD of the initial condition matrix collected around the OTD evolution starting time.

Appendix B. Most amplified initial perturbation

After acquiring knowledge about transient amplifications from spatial modes, we can identify which perturbation has the maximum impact on the disturbed flows. This information is crucial for understanding the underlying mechanisms driving flow

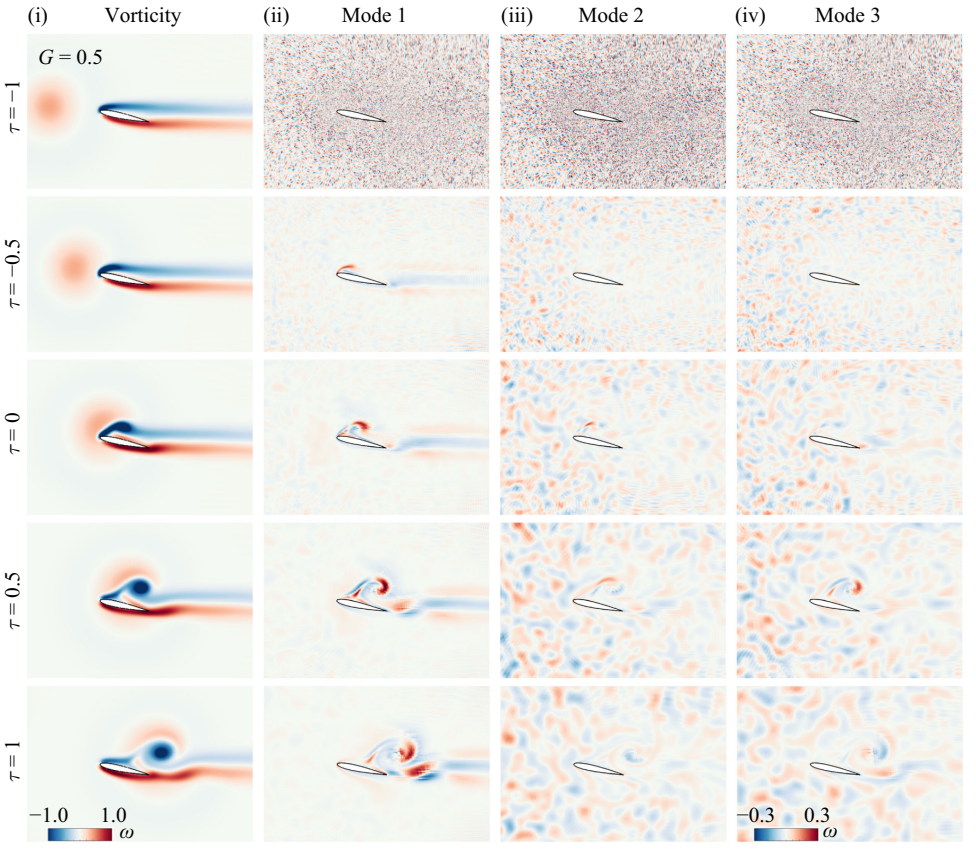

Figure 13. The evolution of OTD modes with random noise as the initial condition, $G = 0.5$.

instabilities and transient growth phenomena. The optimal initial perturbation that leads to the maximum amplification at time τ^* is obtained via (2.18). Starting from τ_0 to τ^*, the most amplified initial perturbation can be written as

$$\mathbf{q}_0'^* = \hat{\mathbf{U}}_r(\tau_0)\boldsymbol{\Sigma}_r(\tau_0)\hat{\mathbf{Y}}_r^{\mathrm{T}}(\tau_0)\hat{\mathbf{y}}_1(\tau^*) \in \mathbb{R}^n, \tag{B1}$$

which leads to a largest singular value at $\sigma_1(\tau^*)$ by evolving $\mathbf{q}_0'^*$ in OTD subspace from τ_0 to τ^*. It is important to note that the optimal initial condition determined via B1) is confined to the space spanned by the columns of $\mathbf{Q}_0' \approx \hat{\mathbf{U}}_r(\tau_0)\boldsymbol{\Sigma}_r(\tau_0)\hat{\mathbf{Y}}_r^{\mathrm{T}}(\tau_0)$.

To show the most amplified perturbation at different τ_0 that arrives at the largest singular value at $\tau^* = 1$, we compare its singular value with the largest singular value from the evolution of the set of perturbations $\mathbf{Q}_r' \equiv \hat{\mathbf{U}}_r(\tau_0 = -1)\boldsymbol{\Sigma}_r(\tau_0 = -1)\hat{\mathbf{Y}}_r^{\mathrm{T}}(\tau_0 = -1)$ in the OTD subspace. The product of the OTD modes and the associated coefficients approximates the evolution of the set of perturbations $\mathbf{Q}_r'$, which is referred to as the baseline case in this section. We present the leading singular value of evolving $\mathbf{Q}_r'$ over time with blue solid lines in figure 14. Starting from four initial conditions at $\tau_0 = -1, -0.5, 0$ and 0.5, the most amplified initial perturbations are identified from $\mathbf{q}_0'^* = \hat{\mathbf{U}}_r(\tau_0)\boldsymbol{\Sigma}_r(\tau_0)\hat{\mathbf{Y}}_r^{\mathrm{T}}(\tau_0)\hat{\mathbf{y}}_1(\tau^* = 1)$. The singular value variations are shown on the left-hand side of figure 14. For the vortex–airfoil interaction cases of $G = \pm 0.5$, the singular values from $\mathbf{q}_0'^*(\tau_0 = -1, -0.5, 0)$ and $\mathbf{q}_0'^*(\tau_0 = 0.5)$ almost collapse with the leading

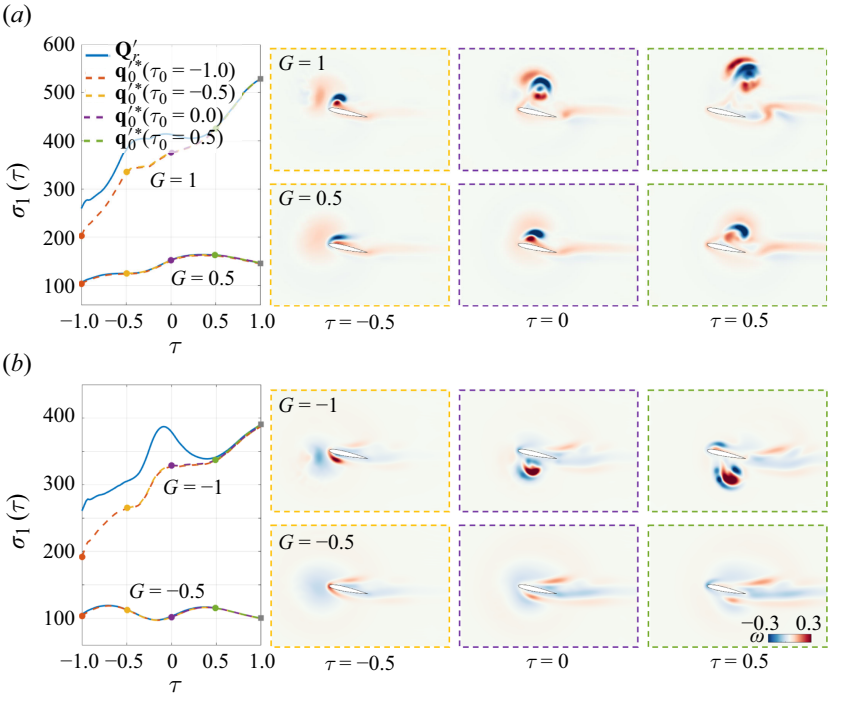

Figure 14. Evolution of the leading singular value subject to different $\mathbf{q}'^*_0$ at $\tau_0=-1$, -0.5, 0, and 0.5 (shown with circles), $\tau^*=1$ (square). The vorticity fields surrounded by yellow, purple and green dashed boxes indicate the most amplified initial perturbations at $\tau_0=-0.5$, 0, and 0.5, respectively. Each perturbation is normalized for visualization.

singular value of evolving the full set of perturbations $\mathbf{Q}'_r$. This result reveals that there exists one single perturbation that can be amplified the most over time. On the other hand, it is observed that the most amplified initial perturbations from cases of $G=\pm1$ have lower singular values than the largest singular value of the baseline case. This suggests that a strong vortex–airfoil interaction The normalized $\mathbf{q}'^*_0$ subject to different τ_0 are shown on the right-hand side of figure 14. For all interaction cases, they follow a similar shape of the leading mode $\hat{\mathbf{u}}_1(t)$, indicating that the regions in which perturbation is amplified the most can be captured by the leading OTD mode.

Moreover, figure 15 presents the most amplified perturbations for a fixed τ_0 and different τ^*. The initial evolution time are the same at $\tau_0=-1$, and the target singular values are at $\tau^*=\tau^*(\sigma_{max})$, -0.5, 0 and 0.5. By comparing the difference between initial perturbations at the same τ_0, we are able to identify the key features of the most dangerous initial perturbation that can be amplified the most over the whole interaction period. For moderate vortex–airfoil interaction cases as presented in figure 15, the singular value variations generally have the same trend as the baseline case. This indicates that the identified $\mathbf{q}'^*_0(\tau_0=-1)$ subject to different τ^* are similar to each other, which can also be visualized on the right-hand side of figure 15. For strong vortex–airfoil interactions, however, the identified $\mathbf{q}'^*_0(\tau_0=-1)$ that leads to a largest singular value of $\tau^*\geq0.5$ possesses a lower singular value than the baseline case. In figure 15, we compare normalized $\mathbf{q}'^*_0(\tau^*(\sigma_{max}))$ with normalized $\mathbf{q}'^*_0(\tau^*=-0.5)$. For strong vortex–airfoil interactions ($G=\pm1$), $\mathbf{q}'^*_0(\tau^*(\sigma_{max}))$ has a higher intensity of vorticity at vortex centre, and $\mathbf{q}'^*_0(\tau^*=-0.5)$ has a sparsely distributed vorticity region in the upstream. This

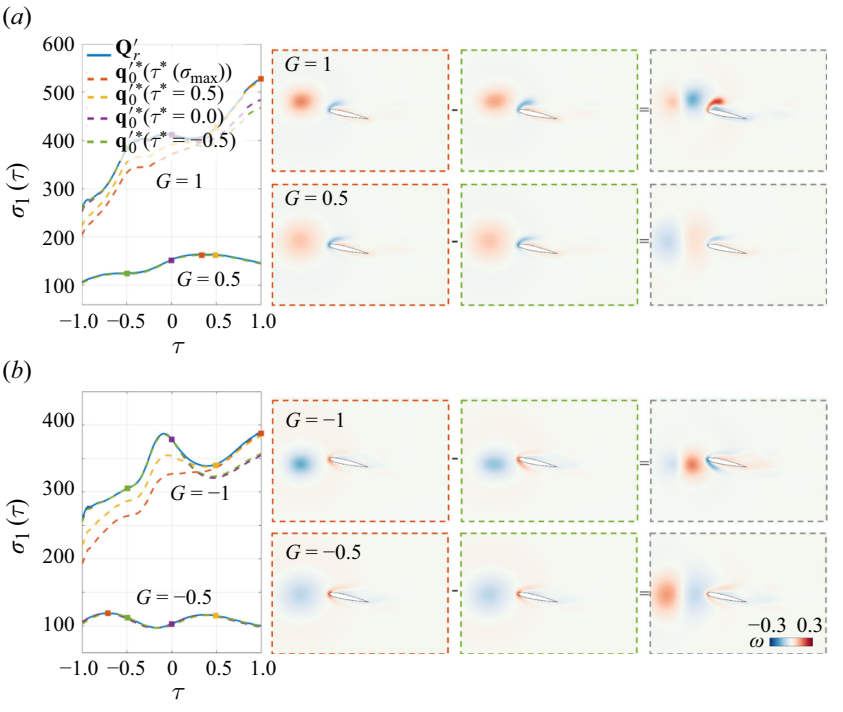

Figure 15. Evolution of the leading singular value subject to different $\mathbf{q}'^*_0$ at $\tau^* = \tau^*(\sigma_{max})$, −0.5, 0, and 0.5 (denoted as squares) with $\tau_0 = -1$. The vorticity fields surrounded by orange, green and grey dashed boxes indicate the most amplified perturbations at $\tau^* = \tau^*(\sigma_{max})$, −0.5, and the difference between them, respectively. Each perturbation is normalized for visualization.

result indicates that a concentrated perturbation on the vortex core upstream is likely to be amplified more than a sparsely distributed perturbation.

In summary, for a time-varying fluid system, the most amplified initial perturbation within the initial perturbation subspace evolves dynamically with time. Identifying these time-dependent, most amplified perturbations through OTD mode analysis highlights the key structures that have the potential to drive significant deviations from the base flow. This understanding is invaluable for perturbation amplification analysis of unsteady fluid systems.

References

Amiri-Margavi, A. & Babaee, H. 2024 Time-dependent low-rank input–output operator for forced linearized dynamics with unsteady base flows. *J. Fluid Mech.* **1001**, A22.

Atassi, H. 1984 The Sears problem for a lifting airfoil revisited - new results. *J. Fluid Mech.* **141**, 109–122.

Aubry, N., Holmes, P., Lumley, J. & Stone, E. 1988 The dynamics of coherent structures in the wall region of a turbulent boundary layer. *J. Fluid Mech.* **192**, 115–173.

Babaee, H., Farazmand, M., Haller, G. & Sapsis, T. 2017 Reduced-order description of transient instabilities and computation of finite-time Lyapunov exponents. *Chaos* **27** (6), 063103.

Babaee, H. & Sapsis, T. 2016 A minimization principle for the description of modes associated with finite-time instabilities. *Phil. Trans. R. Soc. Lond. A* **472** (2186), 20150779.

Badrya, C., Biler, H., Jones, A. & Baeder, J. 2021 Effect of gust width on flat-plate response in large transverse gust. *AIAA J.* **59** (1), 49–64.

Beneitez, M., Duguet, Y., Schlatter, P. & Henningson, D. 2023 Instability of the optimal edge trajectory in the Blasius boundary layer. *J. Fluid Mech.* **971**, A42.

Blackburn, H., Barkley, D. & Sherwin, S. 2008 Convective instability and transient growth in flow over a backward-facing step. *J. Fluid Mech.* **603**, 271–304.

BLANCHARD, A. & SAPSIS, T. 2019*a* Analytical description of optimally time-dependent modes for reduced-order modeling of transient instabilities. *SIAM J. Appl. Dyn. Syst.* **18** (2), 1143–1162.
BLANCHARD, A. & SAPSIS, T. 2019*b* Stabilization of unsteady flows by reduced-order control with optimally time-dependent modes. *Phys. Rev. Fluids* **4** (5), 053902.
BRES, G., HAM, F., NICHOLS, J. & LELE, S. 2017 Unstructured large-eddy simulations of supersonic jets. *AIAA J.* **55** (4), 1164–1184.
DI ILIO, G., CHIAPPINI, D., UBERTINI, S., BELLA, G. & SUCCI, S. 2018 Fluid flow around NACA 0012 airfoil at low-Reynolds numbers with hybrid lattice Boltzmann method. *Comput. Fluids* **166**, 200–208.
DICKINSON, M. & GÖTZ, K. 1993 Unsteady aerodynamic performance of model wings at low Reynolds numbers. *J. Expl Biol.* **174** (1), 45–64.
DONELLO, M., CARPENTER, M. & BABAEE, H. 2022 Computing sensitivities in evolutionary systems: a real-time reduced order modeling strategy. *SIAM J. Sci. Comput.* **44** (1), A128–A149.
ELDREDGE, J. & JONES, A. 2019 Leading-edge vortices: mechanics and modeling. *Annu. Rev. Fluid Mech.* **51** (1), 75–104.
FARRELL, B. & IOANNOU, P. 1993 Stochastic forcing of the linearized Navier–Stokes equations. *Phys. Fluids* **5** (11), 2600–2609.
FUKAMI, K. & TAIRA, K. 2023 Grasping extreme aerodynamics on a low-dimensional manifold. *Nat. Commun.* **14** (1), 6480.
GÓMEZ, F., BLACKBURN, H., RUDMAN, M., SHARMA, A. & MCKEON, B. 2016 A reduced-order model of three-dimensional unsteady flow in a cavity based on the resolvent operator. *J. Fluid Mech.* **798**, R2.
JONES, A. 2020 Gust encounters of rigid wings: taming the parameter space. *Phys. Rev. Fluids* **5** (11), 110513.
JONES, A., CETINER, O. & SMITH, M. 2022 Physics and modeling of large flow disturbances: discrete gust encounters for modern air vehicles. *Annu. Rev. Fluid Mech.* **54** (1), 469–493.
JOVANOVIĆ, M. & BAMIEH, B. 2005 Componentwise energy amplification in channel flows. *J. Fluid Mech.* **534**, 145–183.
KERN, J., HANIFI, A. & HENNINGSON, D. 2022 Subharmonic eigenvalue orbits in the spectrum of pulsating Poiseuille flow. *J. Fluid Mech.* **945**, A11.
KERN, J., NEGI, P., HANIFI, A. & HENNINGSON, D. 2024 Onset of absolute instability on a pitching aerofoil. *J. Fluid Mech.* **988**, A8.
KHALIGHI, Y., HAM, F., MOIN, P., LELE, S. & SCHLINKER, R. 2011*a* Noise prediction of pressure-mismatched jets using unstructured large eddy simulation. In American Society of Mechanical Engineers (ASME) (ed.), *Turbo Expo: Power for Land, Sea, and Air*, vol. **54617**, pp. 381–387.
KHALIGHI, Y., HAM, F., NICHOLS, J., LELE, S. & MOIN, P. 2011*b* Unstructured large eddy simulation for prediction of noise issued from turbulent jets in various configurations. In American Institute of Aeronautics and Astronautics (AIAA) (ed.), *17th AIAA/CEAS aeroacoustics conference (32nd AIAA aeroacoustics conference)*, p. 2886.
KOCH, O. & LUBICH, C. 2007 Dynamical low-rank approximation. *SIAM J. Matrix Anal. Applics.* **29** (2), 434–454.
KURTULUS, D. 2016 On the wake pattern of symmetric airfoils for different incidence angles at re = 1000. *Intl. J. Micro Air Vehicles* **8** (2), 109–139.
KÜSSNER, H. 1936 Zusammenfassender bericht über den instationären auftrieb von flügeln. *Luftfahrtforschung* **13**, 410.
LIU, Q., SUN, Y., YEH, C., UKEILEY, L., CATTAFESTA, L. & TAIRA, K. 2021 Unsteady control of supersonic turbulent cavity flow based on resolvent analysis. *J. Fluid Mech.* **925**, A5.
LIU, Y., LI, K., ZHANG, J., WANG, H. & LIU, L. 2012 Numerical bifurcation analysis of static stall of airfoil and dynamic stall under unsteady perturbation. *Commun. Nonlinear Sci. Numer. Simul.* **17** (8), 3427–3434.
LUMLEY, J. 1967 The structure of inhomogeneous turbulent flows. *Atmos. Turbul. Radio Wave Propag.* 166–178.
MARTÍNEZ-MURIEL, C. & FLORES, O. 2020 Analysis of vortical gust impact on airfoils at low Reynolds number. *J. Fluids Struct.* **99**, 103138.
MCKEON, B. & SHARMA, A. 2010 A critical-layer framework for turbulent pipe flow. *J. Fluid Mech.* **658**, 336–382.
MOARREF, R., SHARMA, A., TROPP, J. & MCKEON, B. 2013 Model-based scaling of the streamwise energy density in high-Reynolds-number turbulent channels. *J. Fluid Mech.* **734**, 275–316.
QIAN, Y., WANG, Z. & GURSUL, I. 2022 Interaction of quasi-two-dimensional vortical gusts with airfoils, unswept and swept wings. *Exp. Fluids* **63** (8), 124.
RAMEZANIAN, D., NOURI, A. & BABAEE, H. 2021 On-the-fly reduced order modeling of passive and reactive species via time-dependent manifolds. *Comput. Meth. Appl. Mech. Engng* **382**, 113882.
ROCKWELL, D. 1998 Vortex-body interactions. *Annu. Rev. Fluid Mech.* **30** (1), 199–229.

SAPSIS, T. & LERMUSIAUX, P. 2009 Dynamically orthogonal field equations for continuous stochastic dynamical systems. *Physica D: Nonlinear Phenom.* **238** (23–24), 2347–2360.

SCHMID, P. 2007 Nonmodal stability theory. *Annu. Rev. Fluid Mech.* **39** (1), 129–162.

SCHMID, P. 2010 Dynamic mode decomposition of numerical and experimental data. *J. Fluid Mech.* **656**, 5–28.

SEARS, W. 1941 Some aspects of non-stationary airfoil theory and its practical application. *J. Aeronaut. Sci.* **8** (3), 104–108.

SUN, Y., TAIRA, K., CATTAFESTA, L. & UKEILEY, L. 2017 Biglobal instabilities of compressible open-cavity flows. *J. Fluid Mech.* **826**, 270–301.

TAIRA, K., BRUNTON, S., DAWSON, S., ROWLEY, C., COLONIUS, T., MCKEON, B., SCHMIDT, O., GORDEYEV, S., THEOFILIS, V. & UKEILEY, L. 2017 Modal analysis of fluid flows: an overview. *AIAA J.* **55** (12), 4013–4041.

TAIRA, K., HEMATI, M., BRUNTON, S., SUN, Y., DURAISAMY, K., BAGHERI, S., DAWSON, S. & YEH, C.-A. 2020 Modal analysis of fluid flows: applications and outlook. *AIAA J.* **58** (3), 998–1022.

TAYLOR, G. 1918 On the dissipation of eddies. *Meteorol. Oceanogr. Turbul. Flow* 96–101.

THEOFILIS, V. 2011 Global linear instability. *Annu. Rev. Fluid Mech.* **43** (1), 319–352.

TREFETHEN, L., TREFETHEN, A., REDDY, S. & DRISCOLL, T. 1993 Hydrodynamic stability without eigenvalues. *Science* **261** (5121), 578–584.

UNNIKRISHNAN, S. 2023 Recent advances in feature extraction techniques for high-speed flowfields. *Prog. Aerosp. Sci.* **140**, 100918.

VON KÁRMÁN, T. & SEARS, W. 1938 Airfoil theory for non-uniform motion. *J. Aeronaut. Sci.* **5** (10), 379–390.

YEH, C. & TAIRA, K. 2019 Resolvent-analysis-based design of airfoil separation control. *J. Fluid Mech.* **867**, 572–610.

ZHONG, Y., FUKAMI, K., AN, B. & TAIRA, K. 2023 Sparse sensor reconstruction of vortex-impinged airfoil wake with machine learning. *Theor. Comput. Fluid Dyn.* **37** (2), 269–287.